Master Thesis

Formation of tidal sand ridges and long bed waves subject to 3D tidal flow

Author:
K.J.H. Lenstra
3144097

Supervisors:
prof. dr. H.E. de Swart
dr. C. Panadés Guinart

Utrecht University

October, 2015

Preface

This study forms my Master of Science Thesis. This thesis is carried out as part of the requirements for the MSc degree in 'Meteorology, Physical Oceanography and Climate' at Utrecht University and it is a result of nine months of research in the field of 'Coastal and Shelf Sea Dynamics' at the Institute for Marine and Atmospheric Research, Utrecht University (IMAU). I would like to thank my supervisors, prof. dr. H.E. de Swart and dr. C. Panadés Guinart, for their support and guidance and the fruitful meetings during this project.

Abstract

Tidal sand ridges and long bed waves are rhythmic bed forms that form as a result from the interaction between the forcing of oscillatory tidal currents and the topography of the bottom. Gaining knowledge of these patterns is important for navigation and to know their response to sand mining. Tidal sand ridges are rotated cyclonically ($5 - 30^o$) with respect to the direction of the tidal current. The typical distance between successive crests is about 10 km. In contrast, crests of long bed waves can be rotated cyclonically ($\sim 60^o$) or anticyclonically ($\sim 30^o$) with respect to the tides and their crest-to-crest distance is about 1.5 km.

Several studies have explained the initial growth and the wavelength and orientation of tidal sand ridges. However, it is unclear why the crests of cyclonic oriented long bed waves are rotated further cyclonically than the crests of tidal sand ridges. One potential explanation for that might be the necessity to account for the vertical structure of the tidal currents. In fact, this is the working hypothesis of this study.

The model used in the present study extends the shallow water equations and introduces a formulation for multiple levels of water. These levels are coupled to the adjacent ones by means of considering the stresses at the interfaces. This assumption allows the vertical structure of the tidal currents to be incorporated in the model. Furthermore, the model includes a sediment transport formulation with a critical bed shear stress below which no sediment moves, as well as the presence of the elliptical tidal currents.

The present work provides new insights in the initial formation of long bed waves and tidal sand ridges, though the main focus is on which tidal conditions allow long bed waves to emerge and how long bed waves form. The results of this study show that the agreement between observed and modelled long bed waves improves when the vertical structure of the tidal currents is included. In fact, the crests of modelled cyclonic oriented long bed waves rotate further cyclonically by $\sim 25^o$ due to Ekman veering and enhanced eccentricity of the tidal ellipse near the seabed.

Contents

1 Introduction **1**
- 1.1 Bed Forms in Tidal Coastal Seas . . . 1
- 1.2 Current State of the Art . . . 3
- 1.3 Purpose of this Study . . . 4
  - 1.3.1 Motivation . . . 4
  - 1.3.2 Research Questions . . . 5
- 1.4 Outline . . . 6

2 Theoretical Concepts **8**
- 2.1 Concepts of Sediment Transport . . . 8
  - 2.1.1 Modes of Transport . . . 8
  - 2.1.2 Threshold of Movement . . . 9
  - 2.1.3 Bed Forms . . . 10
  - 2.1.4 Bed Shear Stress . . . 10
  - 2.1.5 Shields Parameter . . . 10
  - 2.1.6 Sediment Transport . . . 10
- 2.2 The Formation Mechanism of Bed Forms . . . 12
  - 2.2.1 Tidal Sand Ridges . . . 12
  - 2.2.2 Long Bed Waves . . . 13
- 2.3 Linear Stability Concept . . . 14

3 Material **17**
- 3.1 Hydrodynamic Module . . . 18
- 3.2 Sediment Transport Module . . . 21
- 3.3 Morphodynamic Module . . . 21

3.4 Simplifications and Parameterizations . . . 22
3.4.1 Assumptions . . . 22
3.4.2 Closure Relationships Hydrodynamic Module . . . 23
3.4.3 Closure Relationships Sediment Transport Module . . . 27
3.4.4 Tidally Averaging . . . 28
3.5 Linear Stability Analysis . . . 29
3.5.1 Obtaining the Basic State Velocities . . . 29
3.5.2 The Growth of the Bed Forms . . . 31

4 Design of Experiments **36**
4.1 Linearization of Bed Shear Stress . . . 37
4.2 Changing Water Depth . . . 38
4.3 Vertical Structure of the Tidal Currents . . . 40
4.3.1 Orientation of Long Bed Waves . . . 40
4.3.2 Formation of Long Bed Waves . . . 40
4.4 Spring-Neap Cycle . . . 41

5 Results **43**
5.1 Linearization of Bed Shear Stress . . . 43
5.2 Changing Water Depth . . . 45
5.3 Vertical Structure of the Tidal Currents . . . 48
5.3.1 Orientation of Long Bed Waves . . . 48
5.3.2 Formation of Long Bed Waves . . . 52
5.4 Spring-Neap Cycle . . . 55

6 Discussion **58**
6.1 Some Remarkable Elements of the Results . . . 58
6.2 Different Values of the Vertical Eddy Viscosity . . . 59
6.3 Model Limitations . . . 60

7 Conclusions **63**
7.1 Linearization of Bed Shear Stress . . . 63
7.2 Changing Water Depth . . . 64
7.3 Vertical Structure of the Tidal Currents . . . 64
7.3.1 Orientation of Long Bed Waves . . . 64
7.3.2 Formation of Long Bed Waves . . . 65
7.4 Spring-Neap Cycle . . . 65

Appendix A Vertical Structure of the Tidal Ellipse **67**

Bibliography **73**

1 Introduction

1.1 Bed Forms in Tidal Coastal Seas

The interaction between tides, sand transport and morphology is easily noticeable for anyone visiting a shallow tidal environment such as the Dutch Wadden Sea. Tidal currents cause continuous displacement of sand and create channels and intertidal flats. Not visible by eye are the fascinating tide-bottom interactions in deeper water, which are the topics of interest in this thesis.

Generally, coastal seas with water depths up to tens of meters are sandy. Due to different types of forcing, the currents in these seas are up to 1 m s^{-1} and often sufficiently strong to erode sand from the bottom. As a result various sorts of bed forms characterise the seas (see classifications of Dyer and Huntley, 1999). Forces exerted at the bottom by tides and waves are the most important drivers of the sand transport in coastal areas. The joint presence of different types of bed forms can be observed, resulting in complex bottom patterns. The presence, as well as the striking regularity of some of these patterns, have puzzled scientists for decades. The present study focuses on two types of bed forms, viz. tidal sand ridges and long bed waves.

Tidal sand ridges, first identified by Off (1963), have typical distance between crests of about 5 to 10 km, with crests several kilometres wide and tens of meters high. As the name indicates, tidal sand ridges form as a result of feedbacks between the tidal current and the sandy bed. Figure 1.1 shows the location of tidal sand ridges in the North Sea. Near the location where the tidal sand ridges are observed in Fig. 1.1, the maximum tidal current is of the order of 1 m s^{-1}, the local water depth is up to 40 m and the sediment of the seabed is characterized by a mean grain size equal to about 0.4 mm.

The crests of tidal sand ridges are generally rotated counterclockwise (angles between 5^o and 30^o) with respect to the principal direction of the tidal current (Huthnance, 1982). Tidal sand ridges hardly move and evolve in a time scale of centuries or more. The latter raises the question of how tidal sand ridges would react to changing sea level. Currently, the North Sea, the offshore shelves in the North Atlantic Ocean (e.g. close to Florida) and the shelves of the

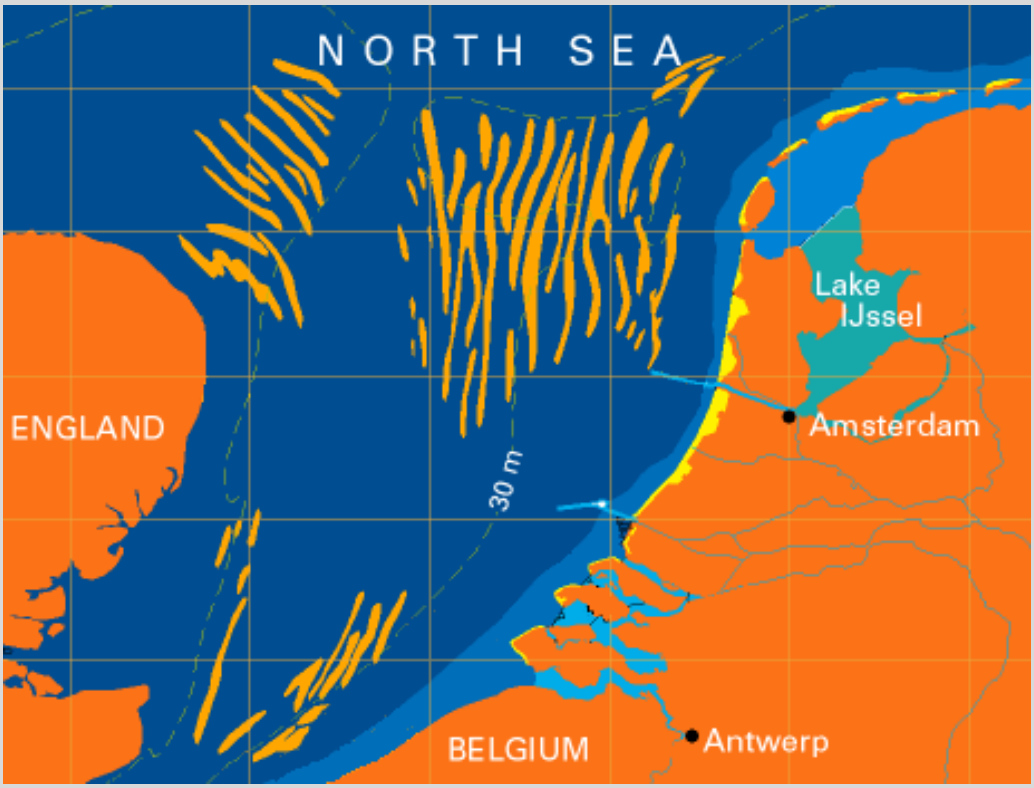

Figure 1.1: Map of tidal sand ridges in the North Sea. The crests of tidal sand ridges are indicated by the orange patches. *After van de Meene (1994).*

China Seas are the hot spots for tidal sand ridge research (Wu et al., 2010).

Long bed waves are bed forms with extents of about 1.5 km. They were observed in the North Sea by Knaapen et al. (2001) and were further described by van Dijk et al. (2008). Like tidal sand ridges, these bed forms have been linked to oscillatory tidal currents, but their evolution in time is not clear. Conditions representative of the coastal area where long bed waves are observed by Knaapen et al. (2001) are circular tides with maximum tidal current of the order of 0.6 m s^{-1}. The typical grain size is equal to about 0.4 mm and the average water depth is 40 m. Long bed waves have crests that are oriented both clockwise (angle $\sim 30^o$) and counterclockwise (angle $\sim 60^o$) with respect to the direction of the dominant tidal current. It is unclear why the crests of counterclockwise oriented long bed waves are rotated further counterclockwise than the crests of tidal sand ridges.

Additional information about the evolution of tidal sand ridges and long bed waves is important for safety of navigation (shipping tracks), the health of the fishing industry and the stability of underwater structures, such as pipelines. Also, tidal sand ridges are considered as potential sources for the extraction of sand, and data suggests that these ridges strongly respond to such interventions (Van Lancker et al., 2010).

1.2 Current State of the Art

Huthnance (1982) was the first to propose such an idealized model in order to gain insight in the relevant physical processes that play a role in the formation of tidal sand ridges. By doing so, he was able to explain the existence of the tidal sand ridges observed in the North Sea, and also explain the properties of these bed forms (length scale, orientation). Several other models have been published as an extension of Huthnance (1982). Relevant literature publications with respect to this study are discussed in the following paragraphs.

The model used by Hulscher et al. (1993) is able to describe both uni-directional and circular (elliptical) tides. Results shows the formation of tidal sand ridges for both cases. By studying a three-dimensional model rather than depth-averaged shallow water equations, Hulscher (1996) was able to account for the differences in ellipticity, amplitude, phase and direction between the depth-averaged flow and the flow just above the bed (driving sediment transport). Hulscher (1996) was able to get a better agreement on the characteristics of tidal sand ridges, such as wavelength and orientations, between her results and field observations.

Blondeaux et al. (2009) showed that long bed waves only form if tidal currents are elliptical and the maximum tidal flow velocity is just above its threshold value for the initiation of sediment motion. The depth-averaged water motion in the used model was supplemented with a more sophisticated sediment transport formulation. In this formulation, it was accounted for the fact that sediment transport only occurs if the velocity is above a certain threshold value.

1.3 Purpose of this Study

1.3.1 Motivation

Bed shear stress is defined as the shear that arises at the interface between the moving water and the seabed, so it is responsible for the bed erosion. In the literature, two types of formulations for the bed shear stress are found. The first one is proportional to the square of the flow velocity, the so-called quadratic bed shear stress. The second formulation is linearly proportional to the flow velocity. This formulation is obtained after applying the procedure described in Lorentz et al. (1926) to the quadratic bed shear stress. For practical purposes, a linear expression for the bed shear stress is often preferred. Here, the effect of the linearization of the bed shear stress on the (modelled) formation of tidal sand ridges and long bed waves is examined and compared to the case of quadratic bed shear stress.

Another important question is related with the fact that tidal sand ridges and long bed waves evolve on a time scale of centuries or more. On this time scale, the local water depth will change. Data suggests that during the last 6000 years the sea-level rise in the North Sea has been between 1 and 4 mm yr^{-1} (Shennan et al., 2000). This would mean changes of several meters in the water depth. The question of how these changes might have affected the initial formation of tidal sand ridges and long bed waves has not been fully addressed.

Regarding the spatial features of long bed waves, while the crest-to-crest distance between successive long bed waves was qualitatively obtained in Blondeaux et al. (2009), so far, the orientation of modelled long bed waves only agrees qualitatively with the observed values. In Blondeaux et al. (2009), the angle between the crests and the tidal current direction was too small: for counterclockwise rotated long bed waves the angle was between 33^o and 14^o and for clockwise rotated long bed waves about 22^o and 16^o. An important simplification of that model was that it did not account for the vertical structure of the tidal currents. As a matter of fact, four properties of the tidal currents depend on the vertical position within a water column.

The first and second are the differences in direction and magnitude between the depth-averaged flow and the flow just above the bed, described by the Ekman spiral. The third one is related with the fact that the tidal current is more elliptical near the bed. The fourth is the difference in phase between the depth-averaged flow and the flow just above the bed. The dependencies of these four properties on the vertical position are hereafter referred to as the vertical structure of the tidal currents. In this study, the working hypothesis is that the vertical structure of the tidal currents can explain the difference between the modelled and observed orientation of long bed waves.

Related to the initial formation of long bed waves, Blondeaux et al. (2009) identified some conditions necessary for the formation of long bed waves. This type of bed forms can only form for weak tidal flow (when the maximum tidal flow velocity is just above the threshold value for erosion) and when the tidal flow is elliptical. Here, it is hypothesised that Ekman veering could also be connected to the formation of these bed forms, so the necessary conditions for long bed wave formation are tested.

In general, the dominant tidal constituent is the semi-diurnal lunar M_2-tide with a period of 12.42 hours. However, there are other constituents that may contribute to the tidal forcing, such as the gravitational pull from the sun. This gives rise to another semi-diurnal constituent, S_2, with a period of 12 hours. The combined effect of the lunar and solar semi-diurnal tides produces what is called the spring-neap cycle, which has a period of 14.79 days. When the sun and moon are at right angles to each other (neap tides) the tidal current velocities are small compared to that during spring tides (when the sun and moon are lined up). In the literature, the models are mainly forced with a single harmonic (only semi-diurnal lunar M_2-tide). The effect of the spring-neap cycle (M_2-tide and semi-diurnal solar S_2-tide) is considered to be negligible or is simply ignored. In this study, the effect of different background tides (single harmonic and spring-neap) on the properties (growth rates, length scale and orientation) of the tidal sand ridges and long bed waves in the initial stages of development is examined.

1.3.2 Research Questions

The previous section is summarized in the following research questions, which are addressed in this study:

1. What is the effect of the linearization of the bed shear stress on the length scale and orientation of tidal sand ridges and long bed waves in the initial stages of development?
2. Are the properties of tidal sand ridges and long bed waves sensitive to changing water depth?
3. (a) Can the vertical structure of the tidal currents explain the difference between modelled and observed orientation of long bed waves?
   (b) Is weak elliptical tidal flow necessary for long bed waves to form?
4. How does the spring-neap cycle affect the properties of the bed forms?

In order to understand and predict geomorphological evolutions in coastal seas a model is needed which describes the dynamics of the water motion, sediment movement and the bed evolution. The first two research questions will be addressed with the model developed and applied by Blondeaux et al. (2009), but adjusted such that the bed shear stress is linearized. To address the remaining research questions, the same model will be extended such that it governs tidal currents at multiple levels, coupled by means of stresses at the interfaces between the levels.

1.4 Outline

The organisation of this thesis is as follows. Chapter 2 covers some important theoretical concepts, used in this study. In Chapter 3, the morphodynamic model is presented. This model consists of three modules: a hydrodynamic module describing the water flow (Section 3.1), a module for the sediment transport (Section 3.2) and the morphodynamic module for the evolution of the seabed (Section 3.3). In Section 3.4, the assumptions, simplifications and parameterizations are discussed. In Section 3.5, the linear stability concept is introduced. The design of the experiments is shown in Chapter 4, and the results obtained in each one of them are in Chapter 5. The experiments are split into four sections, such that the four research questions are covered in individual sections. In Chapter 6, there is the discussion, containing some remarkable aspects of the results, as well as some model limitations. The thesis ends with the conclusions in Chapter 7. Appendix A shows how the characteristics of the tidal ellipse are obtained.

2 Theoretical Concepts

In this chapter, some theoretical concepts will be discussed. The first topic is sediment transport, being crucial for the formation of tidal sand ridges and long bed waves. Secondly, the formation mechanism of tidal sand ridges and long bed waves is presented. In this study, the formation of tidal sand ridges and long bed waves is modelled using linear stability analysis and the theory of this concept is also given.

2.1 Concepts of Sediment Transport

2.1.1 Modes of Transport

There are different types of sediment transport (see Fig. 2.1) and in this section it is considered that sediment particles or grains may be transported in one of the two principal modes:

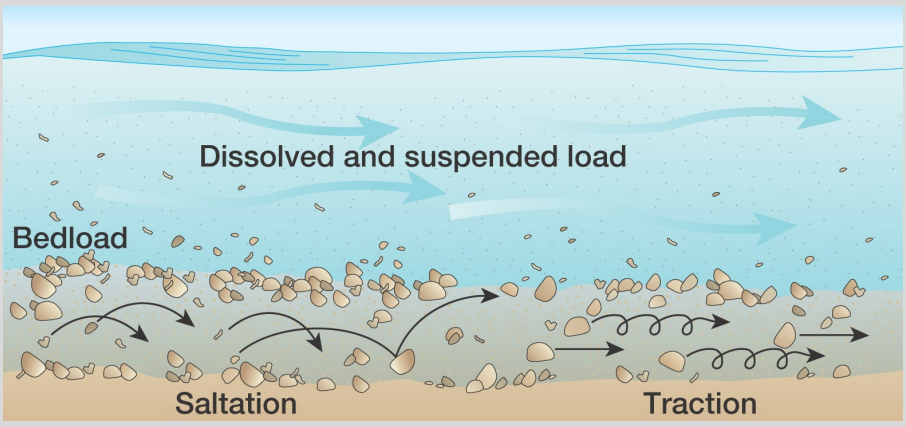

Figure 2.1: A graphic representation of the principal modes of sediment transport. *Source: Paerson Prentice Hall Website.*

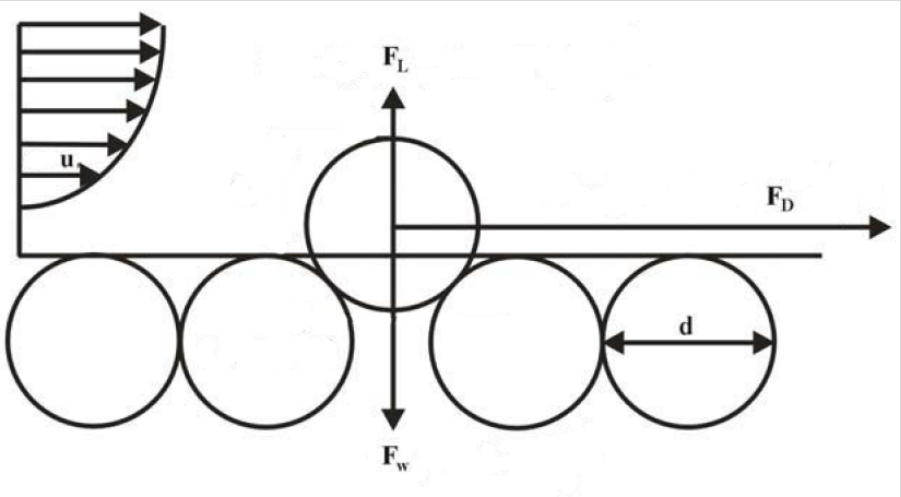

Figure 2.2: A side view of sediment particles with diameter d resting on a seabed. The tidal currents are indicated by u. The stabilising gravitational, lift and drag forces are indicated by F_W, F_L and F_D, respectively. *After Dyer (1986).*

1. by rolling, saltating or sliding along the bed of the sea, sediment remains in contact with the bed, thus transported as bedload;
2. by suspension in the moving water which is the suspended load.

Here, sediment is cohesionless sand. Bedload transport usually is the dominant mode for low flow velocities. Conversely, high flow velocity is a necessary condition for suspended load transport to occur (Reeve et al., 2004). Other modes, such as washload (particles in suspension whose origin is not from the bed, but for instance come from river systems) and sheetflow (when the bedload comprises several layers of moving particles, all in contact with one another), are not considered here.

2.1.2 Threshold of Movement

A perfectly round object lying on a smooth horizontal surface will readily roll on application of a horizontal force. In the case of an erodible boundary as the seabed, the particles are not perfectly round, and they lie on a surface which is inherently rough. An example can be seen in Fig. 2.2, where three forces act on a sediment particle. The first force is caused by the weight of the sediment particle and is the stabilising gravitational force. Shear stress of the bed with the water motion, called bed shear stress τ_b, results in the lift force and the drag force. Thus, the water motion will only cause sediment motion if the combination of lift and drag forces is sufficient to overcome the stabilising gravitational forces. If the bed shear stress is gradually increased from zero, a point is reached at which particle start to move as bedload. This point is described as the threshold of motion and is associated with a critical bed shear stress τ_{cr}.

2.1.3 Bed Forms

Once the bed shear stress is sufficient to cause sediment transport, the seabed can begin to alter its form producing a pattern of bed forms depending on the nature of the flow. For the case of a uniform current originating from tides, ripples will initially form in the bed. These ripples may grow into larger dunes (such as tidal sand ridges or long bed waves for tidal currents). Bed forms cause frictional resistance to the flow in addition to that caused by grain roughness and play a crucial role in the estimation of the total bed shear stress.

2.1.4 Bed Shear Stress

According to the previous paragraph, the two main contributions to the total bed shear stress are:

1. the skin friction or grain-related friction (τ_s);
2. the form drag resulting from ripples on the bed (τ_f).

Hence, the total bed shear stress is given by

$$\tau_b = \tau_s + \tau_f. \tag{2.1}$$

Only the skin friction bed shear stress acts directly on the sediment particles and thus this parameter must be used when calculating the bedload sediment transport.

2.1.5 Shields Parameter

The Shields parameter θ, also known as the entrainment function, is defined as the ratio of destabilising force due to skin friction and stabilising gravitational force (Shields, 1936), i.e.

$$\theta = \frac{\tau_s}{(\rho_s - \rho)gd}, \tag{2.2}$$

where ρ_s is the density of sediment, ρ the density of water, g the acceleration due to Earth's gravity and d the sediment grain size. At the threshold of movement, this becomes the critical Shields parameter

$$\theta_{cr} = \frac{\tau_{cr}}{(\rho_s - \rho)gd}. \tag{2.3}$$

2.1.6 Sediment Transport

If $\theta < \theta_{cr}$, then no sediment transport will occur: the flow velocity is too low to cause a shear stress strong enough to overcome the stabilising gravitational effects. If $\theta \geq \theta_{cr}$, then sediment transport will occur. With increasing shear between water and bed (increased water motion), the Shields parameter increases and so does the sediment transport rate. Various sediment

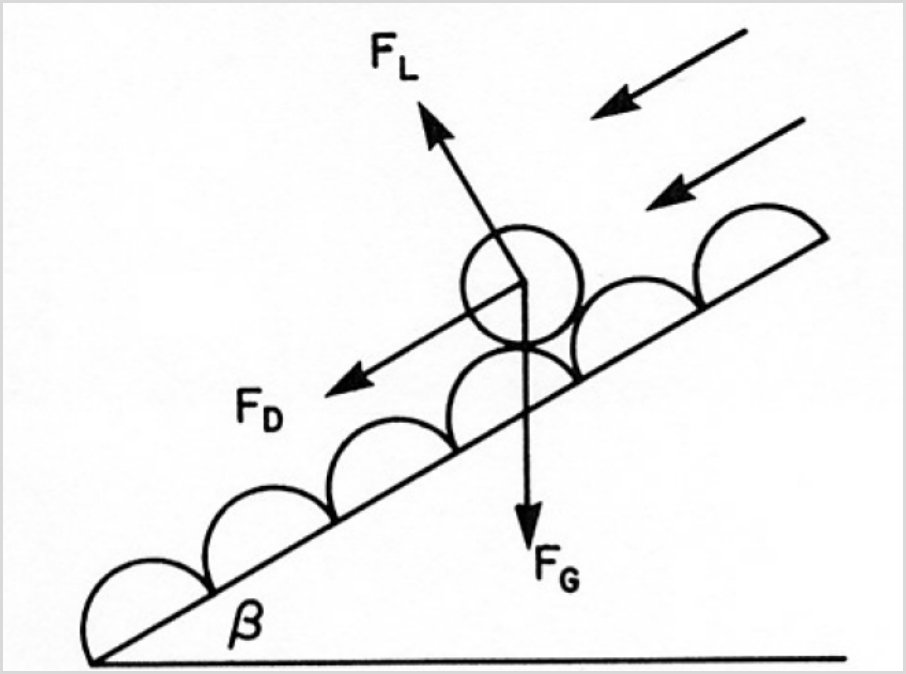

Figure 2.3: A side view of sediment particles with diameter d resting on a seabed inclined by angle β. The gravitational, lift and drag forces are indicated by F_G, F_L and F_D, respectively. *After Dyer (1986).*

transport equations have been developed. Experiments show that the relation between Shields parameter θ and the sediment transport rate Q is not linear (e.g. Meyer-Peter and Müller, 1948, Kovacs and Parker, 1994).

In the absence of slopes in the sea bed, the sediment transport is aligned with the bed shear stress. However, if the sea bed is inclined (as in Fig. 2.3), the direction of particle motion may deviate slightly from the direction of the local skin friction. This is due to the fact the sediment is transported easier downhill than uphill. A slope in the bed perpendicular to the water motion causes a deviation in the direction of sediment transport. The magnitude of sediment particles is affected by the bed slope both in the direction parallel and perpendicular to the direction of water motion.

2.2 The Formation Mechanism of Bed Forms

2.2.1 Tidal Sand Ridges

Zimmerman (1981) gave a conceptual physical explanation of why tidal sand ridges have slightly counterclockwise turned crests with respect to the tidal current direction. Following his reasoning, when a tidal current crosses a ridge, as shown in Fig. 2.4, the flow is accelerated going up the slope and decelerating going down the slope. Subsequently, two forces act on a water

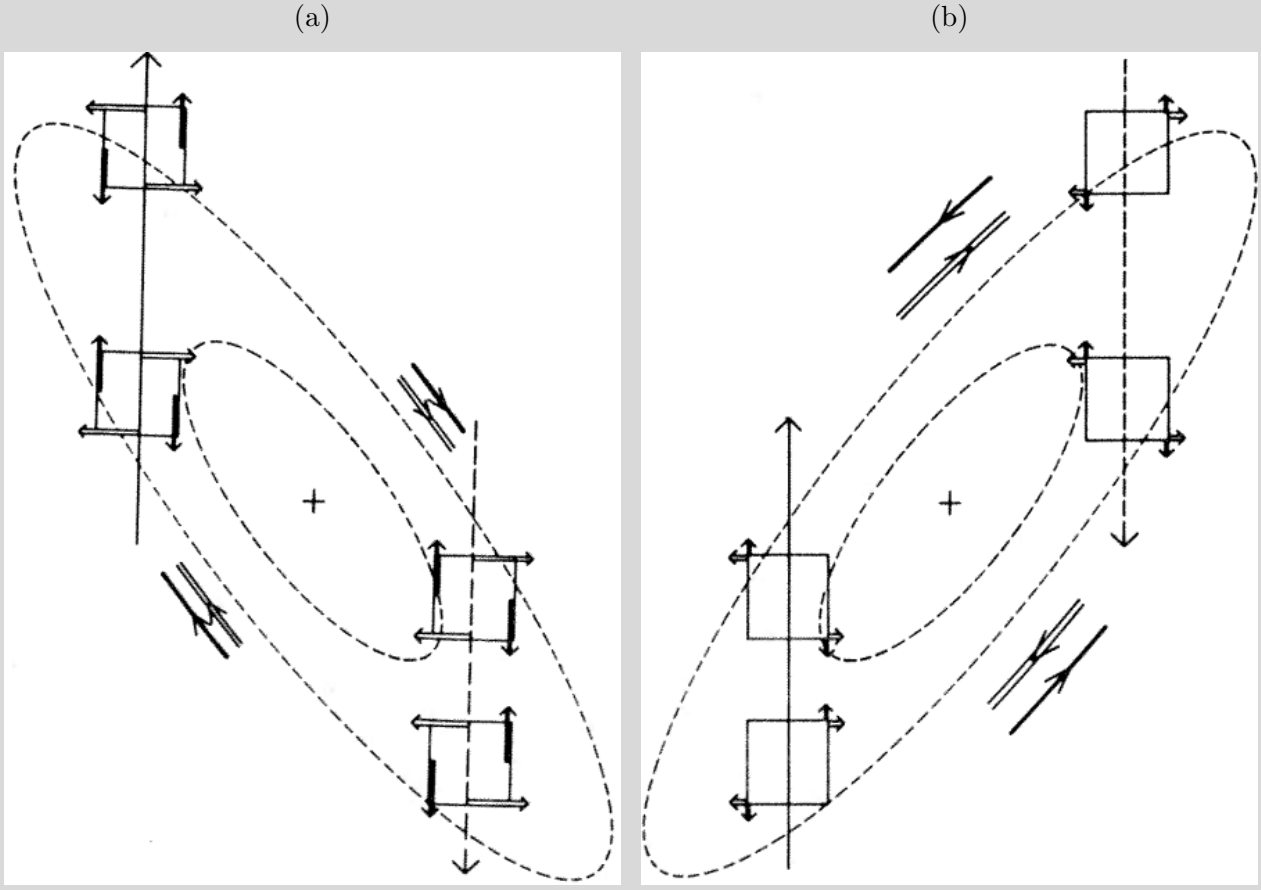

Figure 2.4: The basic production mechanism of residual circulation in tidal currents through Coriolis and bottom frictional torques. The tidal sand ridges are shown by ellipsoidal dashed depth contours; + represents the top of the ridge. Rectilinear tidal currents are represented by solid (dashed) arrows for the flood (ebb) period arrows for the period. The torques acting on a water column due to the Coriolis force and the bottom friction are shown as open and solid arrows, respectively. The resulting residual circulation around the ridge is shown by arrows parallel to the depth contours. (a) Ridge rotated counterclockwise with respect to the current; (b) Ridge rotated clockwise with respect to the current. *(Source: Zimmerman, 1981).*

column that will produce torques: the Coriolis force and the bottom friction.

When accelerating uphill, the faster front end of the water column will experience a stronger Coriolis force than the slower back end of the water column. The front end will therefore be accelerated relatively more towards the right (on the Northern Hemisphere) and the back end relatively more towards the left, i.e. a clockwise 'Coriolis torque' exists on the column. During the deceleration on the other side of the ridge, the opposite happens and an counterclockwise Coriolis torque is produced. This effect is independent of the orientation of the ridge, in other words, this effect occurs for ridges with both clockwise and counterclockwise rotated crests.

A torque is also produced by bottom friction, being stronger at the shallower side of a water column. For an counterclockwise rotated ridge, the right side of the water column is in deeper water than the left side of the water column and thus experiences a relative deceleration. The left side experiences a relative acceleration with respect to the right side and a clockwise 'friction torque' is produced. A water column above a clockwise rotated ridge has the shallower side on the left and thus an counterclockwise 'bottom friction torque' is experienced by the water column.

Both torques reinforce each other if the ridge is inclined counterclockwise with respect to the tidal current (Fig. 2.4a). Clockwise torque is transported towards the ridge and anticlockwise torque is transported from the ridge. The result is clockwise residual circulation around the ridge, which enhances the flow going uphill, allowing more sediment to be transported uphill, and weakens the flow going down the slope, decreasing the sediment removed from the ridge. This results in accumulation of sand at the crests. The two torques counteract in the opposite case (Fig. 2.4b). As a result, a weaker net circulation may be expected and thus the ridges are less likely to grow.

2.2.2 Long Bed Waves

The physical explanation described above can be applied only if transport of sediment occurs ($\theta \geq \theta_{cr}$) during the major part of a tidal cycle, which is the case for strong tidal currents. Under these circumstances, the time averaged circulation over the whole tidal cycle (residual flow) is clockwise around the crests around the crests of the bed forms.

Blondeaux et al. (2009) argued that if tidal currents are weak, it is important for computing net sediment transport that the average circulation is considered over the subintervals of the tidal cycle during which the sea bed is active. The residual flow calculated during the full tidal cycle may differ considerably from that during the intervals that sediment is transported. For certain bed forms, the circulation can be clockwise for the residual flow averaged over the whole tidal cycle and counterclockwise for the residual flow averaged over the phases of the cycle with active sea bed. Blondeaux et al. (2009) showed that the counterclockwise residual flow can form clockwise oriented long bed waves if the tidal currents are elliptical. Hence, both clockwise and counterclockwise rotated long bed waves can grow.

2.3 Linear Stability Concept

Linear stability analysis is a tool that is used to explain the presence of tidal sand ridges and long bed waves. First, a model is needed with equations for tides, sediment transport and bed level. Next, a basic state in this model is defined which describes a tidal current in a shallow sea with uniform water depth.

The stability of this basic state is tested with the introduction of bed perturbations with arbitrary wavelength (distance between successive crests) and angle with the tidal current. A side view of the situation is in Fig. 2.5. The bed perturbation will cause a perturbation is the tidal currents (blue arrows). As a result, additional sediment transport (black arrows) will occur. If the additional sediment transport converges at the crests of the original bed perturbation, giving a positive feedback to the perturbation and the amplitude of the bed perturbation will increase exponentially in time (red arrow). In some cases, the bed perturbation can migrate as a result of asymmetries in the tidal currents.

The basic state is said to be unstable if there is at least one combination of wavelength and angle with the tidal current for which the bed perturbation grows. If (and only if) all possible bed perturbations decay exponentially, the basic state is said to be stable. If the basic state is unstable, linear stability analysis determines the wavelength and orientation for which growth is maximum. This information determines the spatial patterns of the fastest growing mode and the growth rate of this mode. As the initial bottom contains bed perturbations with arbitrary wavelength and orientation, it is expected that the fastest growing mode will dominate over all other modes and thus set the characteristics of the bottom pattern.

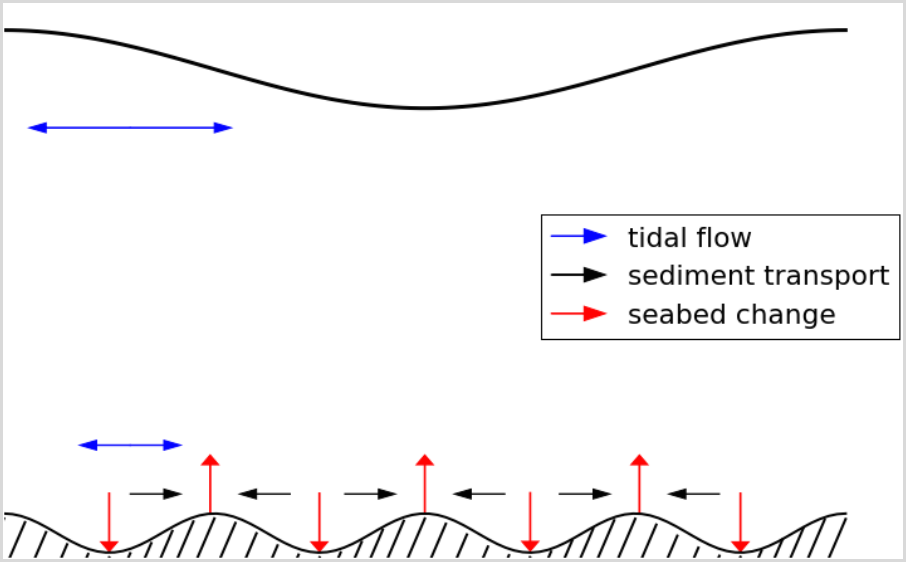

Figure 2.5: Side view of the growth (red arrows) of a bed perturbation (oscillating sea bed) as a result of perturbations in the tidal flow (bleu arrows) that cause additional sediment transport (black arrows).

As the name indicates, nonlinear effects are neglected in the linear stability analysis. Hence, using this analysis gives insight in the mechanism triggering the growth of bed perturbations forced by the propagation of a tidal wave and provides information about some of their initial characteristics, such as wavelength, angle between crests and tidal current, migration speed and initial growth rate. If bed perturbations have become large enough, nonlinear effects can no longer be neglected. Therefore, linear stability analysis can not predict the final height of the bed form, nor the time necessary to attain this final state.

3 Material

This chapter presents, a model that is used to simulate the formation of tidal sand ridges and long bed waves. This model describes the coupling between a tidally-driven water motion and an underlying erodible bed. In particular, the development of a perturbed bed configuration under influence of a tidal flow is investigated with this model, which consists of three coupled parts, i.e. (1) a hydrodynamic module describing the water motion driven by the tides, (2) a module describing the sediment transport and (3) a module for the evolution of the seabed. Figure 3.1 presents an overview of how there modules are coupled.

In the following sections the formulation of the model is discussed, followed by the formulation of linear stability, which is divided in two parts: the definition of the basic state and the development of bed perturbations.

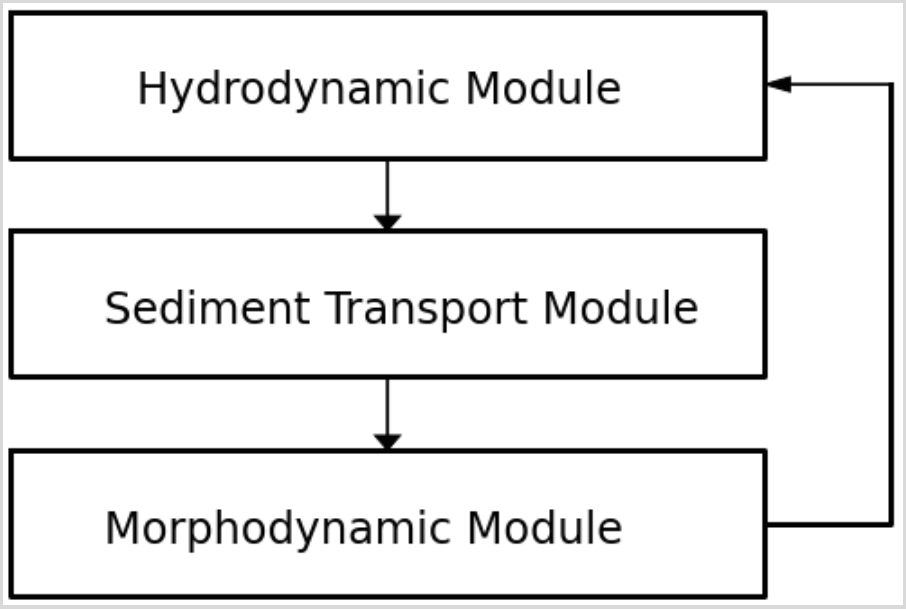

Figure 3.1: The three coupled modules of the model used in this study.

3.1 Hydrodynamic Module

For the problem, a tidal sea is considered with the boundaries infinitely far away. This means that the model considers situations far offshore. The undisturbed water depth H (see Fig. 3.2) is much smaller than the horizontal scale of the problem, justifying the shallow water approximation.

Water motion driven by the tides is described by the shallow water equations. Here, the shallow water equations are formulated for water motion with constant density in a domain that consists of an arbitrary number of vertical levels. A sketch of the situation is shown in Fig. 3.2.

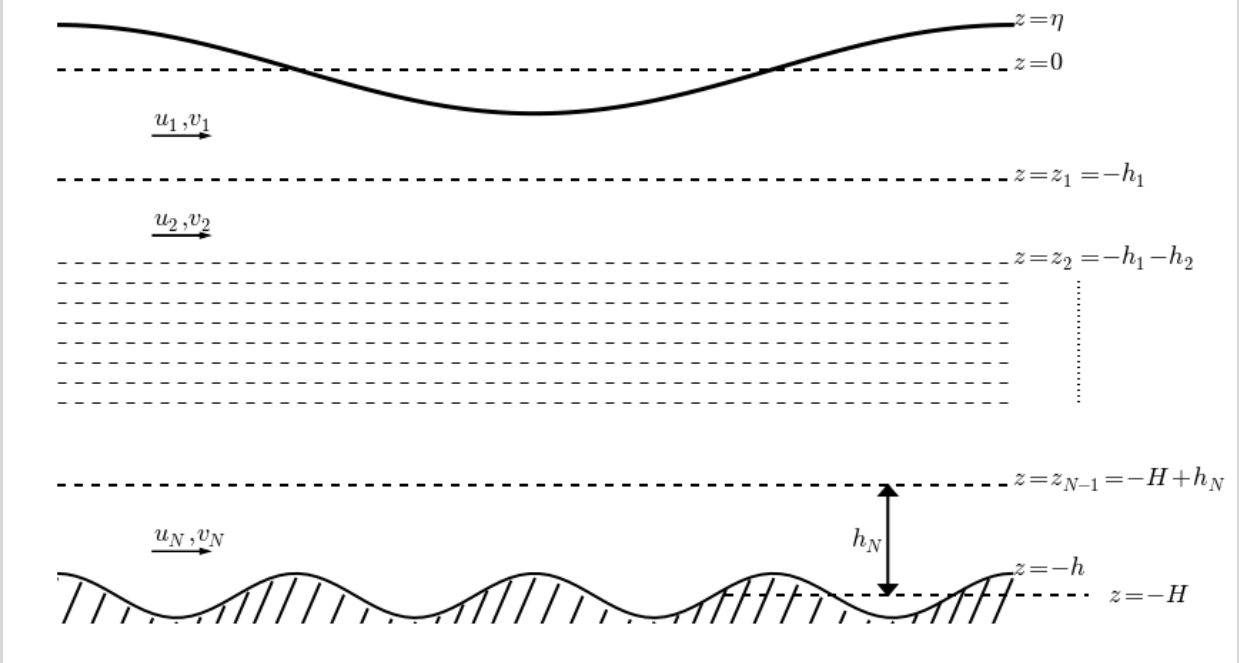

Figure 3.2: Situation sketch of the hydrodynamic module with N levels (side view). Here, (u_i, v_i) with $i = 1, 2, \ldots, N$ are the $(x-, y-)$components of the flow velocity averaged within the level with fixed depth h_i. The vertical coordinate z ranges from $z = -H$, where H is the undisturbed water depth, to $z = \eta$, where η is the elevation of the sea surface. Also, $z = -h$ described the bed profile. The interfaces are fixed at $z = z_j$ with $j = 1, 2, \ldots, N-1$.

The momentum and continuity equations for the top level (indicated by the subscript '1') are

$$\frac{\partial u_1}{\partial t} + u_1\frac{\partial u_1}{\partial x} + v_1\frac{\partial u_1}{\partial y} - fv_1 = -g\frac{\partial \eta}{\partial x} + \frac{1}{\rho(h_1+\eta)}[\tau_{ax} - \tau_{1x}] + \\ + \frac{1}{\rho(h_1+\eta)}\left(\frac{\partial}{\partial x}[(h_1+\eta)\tau_{xx,1}] + \frac{\partial}{\partial y}[(h_1+\eta)\tau_{yx,1}]\right), \tag{3.1a}$$

$$\frac{\partial v_1}{\partial t} + u_1\frac{\partial v_1}{\partial x} + v_1\frac{\partial v_1}{\partial y} + fu_1 = -g\frac{\partial \eta}{\partial y} + \frac{1}{\rho(h_1+\eta)}[\tau_{ay} - \tau_{1y}] + \\ + \frac{1}{\rho(h_1+\eta)}\left(\frac{\partial}{\partial x}[(h_1+\eta)\tau_{xy,1}] + \frac{\partial}{\partial y}[(h_1+\eta)\tau_{yy,1}]\right). \tag{3.1b}$$

$$0 = \frac{\partial \eta}{\partial t} + \frac{\partial}{\partial x}[(h_1+\eta)u_1] + \frac{\partial}{\partial y}[(h_1+\eta)v_1]. \tag{3.1c}$$

Likewise, for the intermediate levels ($i = 2, 3, \ldots, (N-1)$ where N is the number of levels),

$$\frac{\partial u_i}{\partial t} + u_i\frac{\partial u_i}{\partial x} + v_i\frac{\partial u_i}{\partial y} - fv_i = -g\frac{\partial \eta}{\partial x} + \frac{1}{\rho h_i}\left(\tau_{(i-1)x} - \tau_{ix} + \frac{\partial}{\partial x}[h_i\tau_{xx,i}] + \frac{\partial}{\partial y}[h_i\tau_{yx,i}]\right), \tag{3.2a}$$

$$\frac{\partial v_i}{\partial t} + u_i\frac{\partial v_i}{\partial x} + v_i\frac{\partial v_i}{\partial y} + fu_i = -g\frac{\partial \eta}{\partial y} + \frac{1}{\rho h_i}\left(\tau_{(i-1)y} - \tau_{iy} + \frac{\partial}{\partial x}[h_i\tau_{xy,i}] + \frac{\partial}{\partial y}[h_i\tau_{yy,i}]\right), \tag{3.2b}$$

$$0 = \frac{\partial}{\partial x}[h_iu_i] + \frac{\partial}{\partial y}[h_iv_i]. \tag{3.2c}$$

Finally, for the bottom level,

$$\frac{\partial u_N}{\partial t} + u_N\frac{\partial u_N}{\partial x} + v_N\frac{\partial u_N}{\partial y} - fv_N = -g\frac{\partial \eta}{\partial x} + \frac{1}{\rho h_N}\left(\tau_{(N-1)x} - \tau_{bx} + \frac{\partial}{\partial x}[h_N\tau_{xx,N}] + \frac{\partial}{\partial y}[h_N\tau_{yx,N}]\right), \tag{3.3a}$$

$$\frac{\partial v_N}{\partial t} + u_N\frac{\partial v_N}{\partial x} + v_N\frac{\partial v_N}{\partial y} + fu_N = -g\frac{\partial \eta}{\partial y} + \frac{1}{\rho h_N}\left(\tau_{(N-1)y} - \tau_{by} + \frac{\partial}{\partial x}[h_N\tau_{xy,N}] + \frac{\partial}{\partial y}[h_N\tau_{yy,N}]\right), \tag{3.3b}$$

$$0 = \frac{\partial}{\partial x}[h_Nu_N] + \frac{\partial}{\partial y}[h_Nv_N]. \tag{3.3c}$$

In Eq. 3.1-3.3, the following parameters (with $i = 1, 2, \ldots, N$ where N is the number of levels) are used:

t	denotes time [s];
x, y, z	Cartesian coordinates, forming a right-handed set with z pointing upward, $z = 0$ corresponding to the undisturbed surface [m];
u_i, v_i	the components of the level-averaged flow velocity in the directions of increasing x, y respectively [m s^{-1}];
τ_{ax}, τ_{ay}	wind stress acting in the $x-$ and $y-$direction, respectively [N m^{-2}];
τ_{bx}, τ_{by}	bed shear stress in the $x-$ and $y-$direction, respectively [N m^{-2}];
τ_{ix}, τ_{iy}	$x-, y-$components of internal stresses due to vertical shear at the interfaces [N m^{-2}];
$\tau_{xy,i} \ldots$	effective lateral stress within the level acting in the y-direction on a plane at right angles to the x-axis [N m^{-2}];
h_i	the undisturbed water depth of the level [m];
η	the elevation of the sea surface [m];
ρ	the density of water [kg m^{-3}];
f	the Coriolis parameter [s^{-1}].

The undisturbed total water depth H is given by

$$H = h_1 + h_2 + \cdots + h_N. \tag{3.4}$$

In the hydrodynamic module described by Eq. 3.1-3.3, the vertical positions of the interfaces between the levels are fixed. By taking $N = 1$, one arrives at the depth-averaged shallow water equations. Note that to close this set of equations, expressions are needed for the stress terms, which will be be presented later.

3.2 Sediment Transport Module

The sediment transport that is considered here is bedload transport, thus as follows from Section 2.1, the bedload sediment transport Q can be split into two contributions. The first, Q_f, describes the sediment transport in the absence of slopes in the bed. The second is the sediment transport, Q_s, added to account for the small bed slopes. Both contributions are a function of the dimensionless Shields parameter θ. The total volumetric sediment transport rate per unit width (in cubic meter per meter per second) is

$$Q = (Q_f + Q_s)\,\mathcal{H}(\theta - \theta_{cr}). \tag{3.5}$$

Here, $\mathcal{H}$ is the Heaviside function such that the sediment is immobile for $\theta < \theta_{cr}$.

3.3 Morphodynamic Module

Sediment continuity governs the evolution of the seabed: convergence (or divergence) of sediment transport causes a rise (or fall) of the bed level. The sediment continuity equation is written in the form

$$\frac{\partial h}{\partial t} = \frac{1}{1-p}\left(\frac{\partial Q_x}{\partial x} + \frac{\partial Q_y}{\partial y}\right), \tag{3.6}$$

with $p = 0.4$ being the porosity of the bed material. Equation 3.6 gives the variation in the total water depth, and thus the change of height of the bed, in meters per second. Note that Q_x and Q_y are the components of the volumetric sediment transport with its magnitude given by Eq. 3.5.

3.4 Simplifications and Parameterizations

In this section, the most relevant assumptions for the model are discussed. Also, at this point, additional relationships are needed to close the model. The closure relationships for the hydrodynamic module are presented, being formulations for the wind shear, the effective lateral stresses, the vertical shear at the interfaces between the levels and the bed shear stress. To close the sediment transport module, an expression for the skin friction and the sediment transport terms are required. Finally, tidally averaging in the morphodynamic module is discussed.

3.4.1 Assumptions

The semi-diurnal lunar M_2-tide with a frequency of $\omega_{M_2} \simeq 1.4\,10^{-4}\ \mathrm{s}^{-1}$ is assumed to be the main forcing mechanism with the maximum depth-averaged tidal flow velocity U_{da}. The equations will be considered on a domain with undisturbed water depth H. There are two length scales involved in this model; one (λ_{M_2}) is the tidal wavelength; the other (L) is the scale on which the seabed varies. Observations show that L is in the order of the tidal excursion ($L \sim U_{da}/\omega_{M_2}$) or smaller. Furthermore, the dispersion relation for a shallow water wave

$$\lambda_{M_2}\omega_{M_2} = 2\pi\sqrt{gH} \tag{3.7}$$

is being used. For typical conditions the tidal wavelength is in the order of hundreds of kilometers, which means that the ratio L/λ_{M_2} between the two length scales is small. Physically, this corresponds to a rigid lid approximation: spatial variations of the tidal wave due to its propagation at the scale λ_{M_2} are neglected to study the generation of bed forms. As a result, the first term on the right-hand-side of Eq. 3.1c is small compared to the other terms and in Eq. 3.1 ($h_1 + \eta$) is replaced by h_1. In other words, the sea level variations themselves are not important, but the spatial gradients result in pressure gradients in the momentum equations. Hereafter, the acceleration due to pressure gradient forces are represented by

$$P_x \equiv -g\frac{\partial \eta}{\partial x}, \qquad\qquad P_y \equiv -g\frac{\partial \eta}{\partial y}. \tag{3.8}$$

The pressure gradients will result in a horizontally uniform tidal current, which only depends on time with the angular frequency ω_{M_2}.

The use of Cartesian coordinates implies that the sea area is of a sufficiently limited extent for the Earth's curvature to be ignored. The Coriolis parameter f depends on the chosen latitude ϕ, i.e. $f = 2\Omega \sin\phi$ with Ω the rotation rate of the Earth ($\Omega = 7.3\,10^{-5}$ rad s^{-1}). It is assumed that ρ and f are constant (homogeneous sea on a f-plane) and that the pressure in the water obeys the hydrostatic law. The seabed is assumed to be composed of a cohesionless sediment of uniform size d and density ρ_s.

3.4.2 Closure Relationships Hydrodynamic Module

Wind Shear

Since wind is not important for the bed forms considered in this study, the tangential stress at $z = 0$ vanishes (no wind is considered), i.e.

$$\tau_{ax} = 0, \qquad \tau_{ay} = 0. \tag{3.9}$$

Effective Lateral Stresses

In the same direction, aAll effective lateral stresses are neglected to keep the problem simple, hence

$$\tau_{xx,i} = \tau_{yx,i} = \tau_{xy,i} = \tau_{yy,i} = 0, \tag{3.10}$$

with $i = 1, 2, \ldots, N$ and N is the number of levels, because they are not relevant for the generation of tidal sand ridges and long bed waves.

Vertical shear

The stresses at the interface due to water in the levels moving at different velocities is modelled after Bowden (1983)

$$\tau_{ix} = \rho A_v \left.\frac{\partial u}{\partial z}\right|_{z_i}, \qquad \tau_{iy} = \rho A_v \left.\frac{\partial v}{\partial z}\right|_{z_i}. \tag{3.11}$$

Here, z_i is the z-value of the interface of the two levels with index i and $i + 1$ (see Fig. 3.2) and A_v the vertical eddy viscosity. The following parameterization will be used for the vertical shear between two adjacent levels:

$$\left.\frac{\partial u}{\partial z}\right|_{z_j} = \frac{u_i - u_{i+1}}{(h_i + h_{i+1})/2}, \qquad \left.\frac{\partial v}{\partial z}\right|_{z_j} = \frac{v_i - v_{i+1}}{(h_i + h_{i+1})/2}. \tag{3.12}$$

The vertical eddy viscosity is assumed to be constant and the parameterization of Bowden (1953) will be used, i.e.,

$$A_v = c_v U_{da} h, \tag{3.13}$$

where c_v is an appropriate constant. Bowden (1953) and Prandle (1982) found values of c_v in the range 0.0025 to 0.0030. Equation 3.11 is replaced by

$$(\tau_{ix}, \tau_{iy}) = \frac{2\rho c_v U_{da} h}{h_i + h_{i+1}} (u_i - u_{i+1}, v_i - v_{i+1}). \tag{3.14}$$

Bed Shear Stress

Both observations and dimensional arguments indicate that bed shear stress experienced by water motion is quadratic in the velocity (Soulsby, 1997). In terms of the depth-averaged velocity (denoted by $^-$), this bed shear stress has components

$$\tau_{b,x} = C_d \rho \bar{u} \sqrt{\bar{u}^2 + \bar{v}^2}, \qquad \tau_{b,y} = C_d \rho \bar{v} \sqrt{\bar{u}^2 + \bar{v}^2}. \tag{3.15}$$

Here, C_d is the drag coefficient for the quadratic friction law. The formulation of C_d is a consequence of the assumption that the horizontal flow has a logarithmic distribution, i.e.

$$C_d^{-1/2} = \frac{1}{\kappa}\left(\ln\left(\frac{h}{z_0}\right) - 1\right) \simeq \frac{1}{\kappa}\ln\left(\frac{11h}{z_r}\right), \tag{3.16}$$

where $z_r = 30 z_0$ is the Nikuradze roughness and $\kappa = 0.4$ the von Kármán's constant. A formulation is used to account for the presence of ripples, this is done by relating the Nikuradse roughness parameter to the particle Reynolds number R_p, which is a function of the sediment grain size d (Soulsby, 1997):

$$z_r = 202\ d\ R_p^{-0.369}, \qquad R_p = \frac{1}{\nu}\sqrt{(\rho_s/\rho - 1) g d^3}, \tag{3.17}$$

where $\nu = 1.4\,10^{-6}$ m^2 s^{-1} is the kinematic viscosity of water.

As done in many studies, the bed shear stress is linearized using the method proposed by Lorentz(Lorentz et al., 1926). The idea behind this procedure is to substitute the quadratic bed shear stress formulation by a linear expression that yields the same tidally averaged dissipation of energy. Based on that, the original quadratic bed shear stress is replaced by a linearized bed shear stress that causes the same energy dissipation, i.e.,

$$\tau_{bx} = \rho C_d |\bar{u}| \bar{u} \quad \rightarrow \quad \rho \gamma_1 \bar{u}, \tag{3.18}$$

for the $x-$component. At this stage, γ_1 is an unknown linear friction coefficient with units [m s^{-1}]. In general, $\gamma_1 = \gamma_1(x, y)$ is space dependent. However, since the velocity field is taken to be horizontally uniform, γ_1 here no longer depends on x and y. The condition when replacing $C_d|u|$ with γ_1 is that the tidally averaged energy dissipation remains constant. The tidally averaged energy dissipation W is defined as

$$W = \frac{1}{2\pi}\int_0^{2\pi} \tau_b \bar{u}\, \mathrm{d}t \equiv \langle \tau_b \bar{u} \rangle. \tag{3.19}$$

So, the Lorentz linearization condition yields

$$\langle C_d |\bar{u}| \bar{u}^2 \rangle = \langle \gamma_1 \bar{u}^2 \rangle. \tag{3.20}$$

In order to find the value of γ_1, it is assumed that the velocity field for rectilinear tide can by written as

$$\bar{u} = U_{da}\cos(\omega t - \phi), \tag{3.21}$$

where ϕ is the phase of the tide. Subtitution in Eq. 3.20 yields

$$\langle C_d U_{da}^3 \,|\cos(\omega t - \phi)|^3 \rangle = \langle \gamma_1 U_{da}^2 \,|\cos(\omega t - \phi)|^2 \rangle. \tag{3.22}$$

Upon application of the identities

$$\int_0^{2\pi} |\cos(\omega t - \phi)|^3 \,\mathrm{d}t = \frac{8}{3}, \qquad \int_0^{2\pi} |\cos(\omega t - \phi)|^2 \,\mathrm{d}t = \pi, \tag{3.23}$$

it follows

$$\gamma_1 = \frac{8}{3\pi} C_d U_{da}. \tag{3.24}$$

Therefore, the linearized bed shear stress is

$$(\tau_{bx}, \tau_{by}) = \rho\gamma_1(\bar{u}, \bar{v}). \tag{3.25}$$

Hereafter, the conductance coefficient will be used rather than the drag coefficient, i.e.

$$C = \frac{1}{\sqrt{C_d}} = \frac{1}{\kappa}\ln\left(\frac{11h}{z_r}\right). \tag{3.26}$$

The conductance coefficient C is related to the better known Chézy coefficient C_z as $C = C_z/\sqrt{g}$ and

$$\gamma_1 = \frac{8}{3\pi}\frac{1}{C^2} U_{da}. \tag{3.27}$$

For a model with an arbitrary number of levels, it is desirable to have an expression in terms of the flow velocity at the bottom level. The characteristics such as the amplitude, direction and time of maximum flow in the bottom level differ from that of the depth-averaged velocity. This should however result in the magnitude of the bottom shear stress independent of the number of levels (i.e., the magnitude remains constant), while the direction of the bed shear stress is in the direction of the bottom level flow. Thus, the bed shear stress is formulated as

$$\tau_{bx} = \rho\gamma_N u_N, \qquad \tau_{by} = \rho\gamma_N v_N, \tag{3.28}$$

where

$$\gamma_N = \frac{8}{3\pi} C_{f,N} U_N. \tag{3.29}$$

Here, U_N and $C_{f,N}$ are the bottom level current amplitude and the drag coefficient related to the bottom level current, respectively. The constraint that the magnitude of the bed shear stress is independent of the number of levels yields the following equality

$$C_{f,N} U_N^2 = \frac{1}{C^2} U_{da}^2. \tag{3.30}$$

So

$$\gamma_N = \frac{8}{3\pi}\frac{1}{C^2}\frac{U_{da}^2}{U_N}. \tag{3.31}$$

Reduced Hydrodynamic Module

The simplifications and parameterizations reduce the shallow water equations for an arbitrary number of level to

$$\frac{\partial u_1}{\partial t} + u_1\frac{\partial u_1}{\partial x} + v_1\frac{\partial u_1}{\partial y} - fv_1 = P_x - \frac{2A_v}{h_1}\frac{u_1 - u_2}{h_1 + h_2}, \tag{3.32a}$$

$$\frac{\partial v_1}{\partial t} + u_1\frac{\partial v_1}{\partial x} + v_1\frac{\partial v_1}{\partial y} + fu_1 = P_y - \frac{2A_v}{h_1}\frac{v_1 - v_2}{h_1 + h_2}, \tag{3.32b}$$

$$0 = \frac{\partial}{\partial x}[h_1 u_1] + \frac{\partial}{\partial y}[h_1 v_1], \tag{3.32c}$$

$$\frac{\partial u_i}{\partial t} + u_i\frac{\partial u_i}{\partial x} + v_i\frac{\partial u_i}{\partial y} - fv_i = P_x + \frac{2A_v}{h_i}\left(\frac{u_{i-1} - u_i}{h_{i-1} + h_i} - \frac{u_i - u_{i+1}}{h_i + h_{i+1}}\right), \tag{3.32d}$$

$$\frac{\partial v_i}{\partial t} + u_i\frac{\partial v_i}{\partial x} + v_i\frac{\partial v_i}{\partial y} + fu_i = P_y + \frac{2A_v}{h_i}\left(\frac{v_{i-1} - v_i}{h_{i-1} + h_i} - \frac{v_i - v_{i+1}}{h_i + h_{i+1}}\right), \tag{3.32e}$$

$$0 = \frac{\partial}{\partial x}[h_i u_i] + \frac{\partial}{\partial y}[h_i v_i], \tag{3.32f}$$

$$\frac{\partial u_N}{\partial t} + u_N\frac{\partial u_N}{\partial x} + v_N\frac{\partial u_N}{\partial y} - fv_N = P_x + \frac{2A_v}{h_N}\frac{u_{N-1} - u_N}{h_{N-1} + h_N} - \frac{\gamma_N}{h_N}u_N, \tag{3.32g}$$

$$\frac{\partial v_N}{\partial t} + u_N\frac{\partial v_N}{\partial x} + v_N\frac{\partial v_N}{\partial y} + fu_N = P_y + \frac{2A_v}{h_N}\frac{v_{N-1} - v_N}{h_{N-1} + h_N} - \frac{\gamma_N}{h_N}v_N, \tag{3.32h}$$

$$0 = \frac{\partial}{\partial x}[h_N u_N] + \frac{\partial}{\partial y}[h_N v_N], \tag{3.32i}$$

with $i = 2, 3, \ldots, (N-1)$ where N is the number of levels.

3.4.3 Closure Relationships Sediment Transport Module

Skin Friction

In Blondeaux et al. (2009) the skin friction is quadratic in the depth-averaged velocity:

$$\tau_{sx} = \rho \frac{1}{C_1^2} \bar{u} \sqrt{\bar{u}^2 + \bar{v}^2}, \qquad \tau_{sy} = \rho \frac{1}{C_1^2} \bar{v} \sqrt{\bar{u}^2 + \bar{v}^2}. \tag{3.33}$$

Here, C_1 is the conductance coefficient due to the sediment grains for a depth-averaged model,

$$C_1 = \frac{1}{\kappa} \left(\ln \left(\frac{h}{z_0} \right) - 1 \right) \simeq \frac{1}{\kappa} \ln \left(\frac{11h}{2.5d} \right), \tag{3.34}$$

with κ the von Kármán's constant and z_0 the roughness height. Also, a simple formulation of a skin friction component of the roughness height is used which was suggested by Soulsby (1997) and reads $z_0 = 2.5d/30$ where it is shown that the roughness is only determined by the size of the sediment grain size d.

Just as for the bed shear stress, it is desirable to have an expression for the skin friction in terms of the flow velocity in the bottom level. The constraint is again that the modulus of the skin friction must be independent of the number of levels. So, assuming the bottom level flow velocity (u_N, v_N) known,

$$\tau_{sx} = \rho \frac{1}{C_N^2} u_N \sqrt{u_N^2 + v_N^2}, \qquad \tau_{sy} = \rho \frac{1}{C_N^2} v_N \sqrt{u_N^2 + v_N^2}. \tag{3.35}$$

Here, C_N is an unknown conductance coefficient for the multiple level model. Thus, the modulus of τ_s in this case is

$$\tau_s = \rho \frac{1}{C_N^2} U_N^2, \tag{3.36}$$

which must equal that of the depth-averaged model of Blondeaux et al. (2009), yielding

$$C_N = C_1 \frac{U_N}{U_{da}}. \tag{3.37}$$

Here, U_{da} and U_N are the maximum depth-averaged and bottom level tidal flow velocity, respectively. How U_{da} and U_N are computed will be discussed later. In the end, Eq. 3.33 becomes

$$\tau_{sx} = \rho \frac{1}{C_1^2} \left(\frac{U_{da}}{U_N} \right)^2 u_N \sqrt{u_N^2 + v_N^2}, \qquad \tau_{sy} = \rho \frac{1}{C_1^2} \left(\frac{U_{da}}{U_N} \right)^2 v_N \sqrt{u_N^2 + v_N^2}. \tag{3.38}$$

The skin friction is converted to the dimensionless Shields parameter via

$$(\theta_x, \theta_y) = \frac{(\tau_x, \tau_y)}{(\rho_s - \rho) g d}. \tag{3.39}$$

Sediment Transport in the Absence of Bed Slopes

The estimate of the transport rate is $\sqrt{(\rho_s/\rho - 1)gd^3}$, first suggested by Einstein (1950) and commonly encountered in the literature ever since. The bedload sediment transport formulation of Fredsøe and Deigaard (1992) is used for Q_f, its components read

$$(Q_{f,x}, Q_{f,y}) = \sqrt{(\rho_s/\rho - 1)gd^3}\frac{30}{\pi\mu_d}(\theta - \theta_{cr})(\sqrt{\theta} - 0.7\sqrt{\theta_{cr}})\frac{(\theta_x, \theta_y)}{\theta}. \tag{3.40}$$

Here, μ_d the friction coefficient of the sediment mixture and

$$\theta = \sqrt{\theta_x^2 + \theta_y^2}. \tag{3.41}$$

Sediment Transport due to Bed Slopes

Following Seminara (1998), Q_s is written as

$$Q_s = Q_f \mathbf{G}\, \nabla_h h. \tag{3.42}$$

Here, in a reference frame where s, n are local along-flow and cross-flow coordinates, respectively, $\mathbf{G}$ is a dimensionless second order 2D tensor, which reads

$$\mathbf{G} = \begin{pmatrix} G_{ss} & G_{sn} \\ G_{ns} & G_{nn} \end{pmatrix} \tag{3.43}$$

where

$$G_{ns} = G_{sn} = 0, \qquad G_{ss} = \frac{\theta_{cr}}{\mu_d}\frac{1}{Q_f}\frac{\mathrm{d}Q_f}{\mathrm{d}\theta}, \qquad G_{nn} = \frac{k_g}{\sqrt{\theta}}. \tag{3.44}$$

In Eq. 3.44, k_g is a empirical factor ranging about 0.5-0.6 (Talmon et al., 1995) and Q_f is the modulus of the sediment transport without bed slopes. Furthermore

$$\nabla_h \equiv \left(\frac{\partial}{\partial s}, \frac{\partial}{\partial n}\right). \tag{3.45}$$

3.4.4 Tidally Averaging

Significant changes of the seabed only occur after a large number of tidal cycles, i.e. the morphodynamic time scale is much longer than the tidal period. This implies that oscillations of the seabed on the tidal time scale have a negligible influence on the evolution of the seabed on the morphodynamic time scale. Therefore, the sediment transport is averaged over the tidal period and Eq. 3.6 is replaced by

$$\frac{\partial h}{\partial t} = \frac{1}{1-p}\left(\frac{\partial \langle Q_x \rangle}{\partial x} + \frac{\partial \langle Q_y \rangle}{\partial y}\right), \tag{3.46}$$

$(\langle Q_x \rangle, \langle Q_y \rangle)$ being the sediment transport averaged over the tidal period.

3.5 Linear Stability Analysis

From a mathematical point of view, linear stability analysis may be formulated as follows. The hydrodynamic module (Eq. 3.32) allows for a basic state which is characterized by a flat horizontal bed and a horizontally uniform velocity field, i.e. $h = H$ and $(u_i, v_i) = (U_{i,0}(t), V_{i,0}(t))$ with $i = 1, 2, \ldots, N$ where N is the number of levels. The velocities in the basic state (denoted by the subscript '0') will have a vertical structure due to the frictional terms in the momentum equations, but are horizontally uniform. The mathematical formulation of the response of the basic state system to a small bed perturbation and the resulting growth/decay of this perturbation follows after the basic state is described.

3.5.1 Obtaining the Basic State Velocities

It is assumed that the total undisturbed water depth is evenly distributed over all levels. In this study, a depth-averaged basic state tidal flow of each tidal constituent with frequency ω is considered that describes an elliptical tidal flow,

$$\frac{1}{N}\sum_{i=1}^{N} U_{i,0}(t) = U_{da}\sin(\omega t)\cos(\alpha) + \varepsilon_{da}U_{da}\cos(\omega t)\sin(\alpha), \tag{3.47a}$$

$$\frac{1}{N}\sum_{i=1}^{N} V_{i,0}(t) = U_{da}\sin(\omega t)\sin(\alpha) - \varepsilon_{da}U_{da}\cos(\omega t)\cos(\alpha), \tag{3.47b}$$

where α is the angle between the major axis of the tidal ellipse and the $x-$axis, and ε_{da} is the eccentricity of the depth-averaged tidal ellipse. Here, $0 \leq |\varepsilon_{da}| \leq 1$ is assumed: $\varepsilon_{da} = 0$ describes an oscillating unidirectional tide, $0 < |\varepsilon_{da}| < 1$ describes elliptical tides and setting $|\varepsilon_{da}| = 1$ yields circular tides. Similar models including a vertical structure have been considered by, e.g. Prandle (1982), Maas and Van Haren (1987) and Hulscher (1996). Expressions for the basic velocities $U_{i,0}$ and $V_{i,0}$, which are functions of time and the level number i, are derived. The basic solution can be presented either in tidal components or in terms of elliptical properties; the former will be used for linear stability analysis (Section 3.5.2) and are discussed here, while the latter are helpful for a physical interpretation and presented in Appendix A.

The total flow is the summation of the different tidal constituents. For the one-level model ($N = 1$), the basic state is given by the right-hand-side of Eq. 3.47. For the multilevel model, the depth-averaged current controls the basic state in all levels. How the depth-averaged currents are distributed over all levels depends, amongst other parameter values, on the value of γ_N, which depends nonlinearly on the amplitude of the bottom level current U_N.

The momentum equations of the basic state for the top level are

$$\frac{dU_{1,0}}{\partial t} - fV_{1,0} = P_x - \mu_N(U_{1,0} - U_{2,0}), \tag{3.48a}$$

$$\frac{dV_{1,0}}{\partial t} + fU_{1,0} = P_y - \mu_N(V_{1,0} - V_{2,0}), \tag{3.48b}$$

with

$$\mu_N = \frac{N^2}{H^2} A_v = \frac{N^2 c_v U_{da}}{H}, \tag{3.49}$$

the momentum equations for the intermediate levels $i = 2, 3, \ldots, (N-1)$

$$\frac{dU_{i,0}}{\partial t} - fV_{i,0} = P_x - \mu_N(2U_{i,0} - U_{(i-1),0} - U_{(i+1),0}), \tag{3.50a}$$

$$\frac{dV_{i,0}}{\partial t} + fU_{i,0} = P_y - \mu_N(2V_{i,0} - V_{(i-1),0} - V_{(i+1),0}), \tag{3.50b}$$

and the momentum equations for the bottom level

$$\frac{dU_{N,0}}{\partial t} - fV_{N,0} = P_x + \mu_N(U_{(N-1),0} - U_{N,0}) - \frac{N}{H}\gamma_N u_{N,0}, \tag{3.51a}$$

$$\frac{dV_{N,0}}{\partial t} + fU_{N,0} = P_y + \mu_N(V_{(N-1),0} - V_{N,0}) - \frac{N}{H}\gamma_N v_{N,0}, \tag{3.51b}$$

with

$$\gamma_N = \frac{8}{3\pi}\frac{1}{C^2}\frac{U_{da}^2}{U_N} \tag{3.52}$$

Equations 3.47-3.52 form a closed set of $N+2$ equations for the $N+2$ unknowns ($U_{i,0}$, $V_{i,0}$, P_x and P_y). Since the problem is nonlinear in Eq. 3.52, the equations are solved iteratively in γ_N. This procedure is shown for $N = 2$, but can be straightforwardly extended for a system with more levels. Note that for $N = 1$, the problem is linear.

First a guess value of γ_2 is tried, i.e. $\gamma_2 = \gamma_1$. The solutions of the forcing and flow components are periodic with frequency of the tide, so can be expressed as

$$\begin{aligned} P_x &= \Re\{\hat{p}_x e^{-\mathrm{i}\omega t}\}, \quad P_y = \Re\{\hat{p}_y e^{-\mathrm{i}\omega t}\}, \\ U_{1,0} &= \Re\{\hat{u}_1 e^{-\mathrm{i}\omega t}\}, \quad V_{1,0} = \Re\{\hat{v}_1 e^{-\mathrm{i}\omega t}\}, \\ U_{2,0} &= \Re\{\hat{u}_2 e^{-\mathrm{i}\omega t}\}, \quad V_{2,0} = \Re\{\hat{v}_2 e^{-\mathrm{i}\omega t}\}. \end{aligned} \tag{3.53}$$

Here, $\mathrm{i} = \sqrt{-1}$. The complex amplitudes (denoted by $\hat{}$) follow from substituting Eq. 3.53 in Eq. 3.47, 3.48, 3.51 and solving the linear system described in matrix form by

$$\begin{pmatrix} \mu_2 - \mathrm{i}\omega & -f & -\mu_2 & 0 & -1 & 0 \\ f & \mu_2 - \mathrm{i}\omega & 0 & -\mu_2 & 0 & -1 \\ -\mu_2 & 0 & 2\gamma_2/H + \mu_2 - \mathrm{i}\omega & -f & -1 & 0 \\ 0 & -\mu_2 & f & 2\gamma_2/H + \mu_2 - \mathrm{i}\omega & 0 & -1 \\ 0.5 & 0 & 0.5 & 0 & 0 & 0 \\ 0 & 0.5 & 0 & 0.5 & 0 & 0 \end{pmatrix} \begin{pmatrix} \hat{u}_1 \\ \hat{v}_1 \\ \hat{u}_2 \\ \hat{v}_2 \\ \hat{p}_x \\ \hat{p}_y \end{pmatrix} = \begin{pmatrix} 0 \\ 0 \\ 0 \\ 0 \\ \hat{u}_{da} \\ \hat{v}_{da} \end{pmatrix}. \tag{3.54}$$

Here,

$$\begin{aligned} \hat{u}_{da} &= \varepsilon_{da} U_{da} \sin(\alpha) + \mathrm{i} U_{da} \cos(\alpha), \\ \hat{v}_{da} &= -\varepsilon_{da} U_{da} \cos(\alpha) + \mathrm{i} U_{da} \sin(\alpha), \end{aligned} \tag{3.55}$$

as is traced back from Eq. 3.47. Note that

$$U_{da} = \sqrt{\frac{|\hat{u}_{da}|^2 + |\hat{v}_{da}|^2}{1 + \varepsilon_{da}^2}}. \tag{3.56}$$

A new value of γ_2 comes from Eq. 3.52 and is substituted in Eq. 3.54. The solution gives a new value of

$$U_2 = \sqrt{\frac{|\hat{u}_2|^2 + |\hat{v}_2|^2}{1 + \varepsilon_2^2}} \tag{3.57}$$

and thus a new value of γ_2 from Eq. 3.52. Recall that

$$\gamma_2 = \frac{8}{3\pi}\frac{1}{C^2}\frac{U_{da}^2}{U_2}. \tag{3.58}$$

Here, ε_2 is the eccentricity of the tidal ellipse described by $(\hat{u}_2, \hat{v}_2)$, as is explained in Appendix A. Note that $\varepsilon_2 \neq \varepsilon_{da}$. The process is re-iterated with substituting γ_2 in Eq. 3.54, yielding a new value of γ_2. Once γ_2 in the beginning of the iteration and the new one are within a certain tolerance (10^{-6}), the iterative procedure is stopped.

3.5.2 The Growth of the Bed Forms

The stability of the basic state is investigated by adding a bed perturbation of small amplitude and investigating the growth or decay of this perturbation. Since the perturbation is assumed to have an infinitesimal amplitude, the problem is linearized: the bed profile is described by the superposition of different spatial components, which evolve independently of each other. Hence, the problem is solved for the generic spatial component of the bed configurations. Here, the $x-$axis is chosen to be aligned with the crests of the bed form so, without loss of generality, a bed profile described by

$$h_N = \frac{H}{N} - H\epsilon[A(t)e^{\mathrm{i}ky} + c.c.]), \quad h = H - H\epsilon[A(t)e^{\mathrm{i}ky} + c.c.] \tag{3.59}$$

is considered. In Eq. 3.59, $\epsilon A(t)$ is the amplitude of the generic component which is periodic in the $y-$direction with an arbitrary wavenumber k. Moreover, *c.c.* indicates the complex conjugate of the preceding term. The parameter ϵ is assumed to be infinitesimally small ($\epsilon \to 0$) and $A(t)$ describes the growth/decay of the bed perturbation. The small value of ϵ allows the solution to be expanded in the form

$$\begin{pmatrix} u_i \\ v_i \\ P_x \\ P_y \\ \gamma_N \end{pmatrix} = \begin{pmatrix} U_{i,0} \\ V_{i,0} \\ P_{x,0} \\ P_{y,0} \\ \gamma_{N,0} \end{pmatrix} + \begin{pmatrix} U_{i,1} \\ V_{i,1} \\ 0 \\ P_{y,1} \\ \gamma_{N,1} \end{pmatrix} \epsilon[A(t)e^{\mathrm{i}ky} + c.c.] + \mathcal{O}(\epsilon^2), \tag{3.60}$$

with $i = 1, 2, \ldots, N$ where N is the number of levels. Moreover, $\gamma_{N,0}$ is the value of γ_N for $h = H$ and

$$\gamma_{N,1} = \frac{40}{3\pi}\frac{1}{C_0^3}\frac{U_{da}^2}{U_N}. \tag{3.61}$$

At the leading order, i.e. $O(\epsilon^0)$, the solution will be described by the basic state velocities. In Eq. 3.60, $(U_{i,0}, V_{i,0})$ are the basic state velocity components described before. The perturbed flow $(U_{i,1}, V_{i,1})$ is governed by the same equations and at order ϵ, the continuity equation in the bottom level (Eq. 3.32i) yields

$$V_{N,1} = NV_{N,0}. \tag{3.62}$$

Similarly, $V_{i,1} = 0$ with $i = 1, 2, \ldots, (N-1)$. The resulting linearized equation in the $x-$direction, after making Taylor expansions of the non-linear terms and including $V_{1,1} = 0$, for the top level is:

$$\frac{\mathrm{d}U_{1,1}}{\mathrm{d}t} = -\mathrm{i}kV_{1,0}U_{1,1} - \mu N^2\left[(U_{1,1} - U_{2,1}) - (U_{1,0} - U_{2,0})\right], \tag{3.63}$$

with

$$\mu = \frac{c_v U_{da}}{H}. \tag{3.64}$$

Likewise, for the intermediate levels

$$\begin{aligned}\frac{\mathrm{d}U_{i,1}}{\mathrm{d}t} = &-\mathrm{i}kV_{i,0}U_{i,1} - \mu N^2\left[(2U_{i,1} - U_{(i+1),1} - U_{(i-1),1})\right. \\ &\left.-(2U_{i,0} - U_{(i+1),0} - U_{(i-1),0})\right], \end{aligned} \tag{3.65a}$$

$$\begin{aligned}\frac{\mathrm{d}U_{(N-1),1}}{\mathrm{d}t} = &-\mathrm{i}kV_{(N-1),0}U_{(N-1),1} - \mu N^2\left[(2U_{(N-1),1} - U_{N,1} - U_{(N-2),1})\right. \\ &\left.-(U_{(N-1),0} - U_{(N-2),0}) + (U_{(N-1),0} - U_{N,0})\left(\frac{N}{2} - 1\right)\right], \end{aligned} \tag{3.65b}$$

with $i = 2, \ldots, (N-2)$. Note that the equation for the lowest intermediate level differs from the other intermediate levels because Eq. 3.32d depends on h_N for $i = (N-1)$, thus giving an additional term. For the bottom level,

$$\begin{aligned}\frac{\mathrm{d}U_{N,1}}{\mathrm{d}t} = NfV_{N,0} - \mathrm{i}kV_{N,0}U_{N,1} + \mu N^2&\left[(U_{(N-1),1} - U_{N,1}) + (U_{(N-1),0} - U_{N,0})\left(\frac{3N}{2} - 1\right)\right] \\ &- \frac{N}{H}\left[\gamma_{N,0}U_{N,1} + U_{N,0}\left(N\gamma_{N,0} + \gamma_{N,1}\right)\right]. \end{aligned} \tag{3.66}$$

The interest is in the non-transient part of the solution $U_{N,1}$, which is numerically determined using the second order Runge-Kutta method. Once the hydrodynamic problem is solved for

the perturbed flow, the sediment transport is expanded as

$$\begin{pmatrix} \tau_x \\ \tau_y \\ \theta_x \\ \theta_y \\ Q_x \\ Q_y \\ C_N \end{pmatrix} = \begin{pmatrix} \tau_{x,0} \\ \tau_{y,0} \\ \theta_{x,0} \\ \theta_{y,0} \\ Q_{x,0} \\ Q_{y,0} \\ C_{1,0} \end{pmatrix} + \begin{pmatrix} \tau_{x,1} \\ \tau_{y,1} \\ \theta_{x,1} \\ \theta_{y,1} \\ Q_{x,1} \\ Q_{y,1} \\ C_{1,1} \end{pmatrix} \epsilon[A(t)e^{\mathrm{i}ky} + c.c.] + \mathcal{O}(\epsilon^2). \tag{3.67}$$

Here, $C_{1,0}$ is the value of C_1 for $h = H$ and $C_{1,1} = -2.5$.

At the leading order no sediment moves, i.e. $\langle Q_{x,0} \rangle = \langle Q_{y,0} \rangle = 0$. The time development of the amplitude $A(t)$ of the generic component of the bed perturbation, which follows from sediment continuity equation (Eq. 3.46), therefore only depends on the $O(\epsilon)$ sediment transport. The result is

$$\frac{\mathrm{d}A(t)}{\mathrm{d}t} = -\frac{\mathrm{i}k}{(1-p)H} \langle Q_{y,1} \rangle A(t) = \Gamma A(t), \tag{3.68}$$

where the variable $\langle Q_{y,1} \rangle$ is the time average of $Q_{y,1}$. The solution of Eq. 3.68 is

$$A(t) = A_0 e^{\Gamma t}. \tag{3.69}$$

The complex growth rate $\Gamma = \Gamma_r + \mathrm{i}\Gamma_i$ depends on the parameters of the problem. Hence, Eqs. 3.59-3.69 give rise to a bed evolution described by

$$h = H(1 - \epsilon A_0 \, e^{\Gamma_r t} \, [e^{\mathrm{i}(ky + \Gamma_i t)} + c.c.]), \tag{3.70}$$

So, Γ_r controls the growth/decay of the bed perturbation and $\Gamma_i = -kc$ is related to the migration of the bed perturbations, where c is the migration phase speed.

The value of $Q_{y,1}$ follows from the contribution the perturbed flow to the skin friction (Eq. 3.38),

$$\begin{aligned} \tau_{x,1} &= \frac{\rho}{C_{1,0}^2} \left(\frac{U_{da}}{U_N} \right)^2 \sqrt{U_{N,0}^2 + V_{N,0}^2} \left[U_{N,1} + U_{N,0} \left(\frac{5}{C_{1,0}} + \frac{U_{N,0}U_{N,1} + V_{N,1}V_{N,0}}{U_{N,0}^2 + V_{N,0}^2} \right) \right], \\ \tau_{y,1} &= \frac{\rho}{C_{1,0}^2} \left(\frac{U_{da}}{U_N} \right)^2 \sqrt{U_{N,0}^2 + V_{N,0}^2} \left[V_{N,1} + V_{N,0} \left(\frac{5}{C_{1,0}} + \frac{U_{N,0}U_{N,1} + V_{N,1}V_{N,0}}{U_{N,0}^2 + V_{N,0}^2} \right) \right]. \end{aligned} \tag{3.71}$$

The components of the Shields parameter at order ϵ are

$$\theta_{x,1} = \frac{\tau_{x,1}}{(\rho_s - \rho)gd}, \tag{3.72a}$$

$$\theta_{y,1} = \frac{\tau_{y,1}}{(\rho_s - \rho)gd}, \tag{3.72b}$$

with order ϵ Shields parameter magnitude defined as

$$\theta_1 = \frac{\theta_{x,1}\theta_{x,0} + \theta_{y,1}\theta_{y,0}}{\theta_0}. \tag{3.73}$$

If

$$\theta_0 = \sqrt{\theta_{x,0}^2 + \theta_{y,0}^2} > \theta_{cr}, \tag{3.74}$$

then $Q_{y,1}$ is computed as follows

$$Q_{y,1} = \sqrt{(\rho_s/\rho - 1)gd^3}\left(\theta_1 \left.\frac{\partial Q_y}{\partial \theta}\right|_{\theta=\theta_0} + \theta_{y,1} \left.\frac{\partial Q_y}{\partial \theta_y}\right|_{\theta_y=\theta_{y,0}} - \left.\frac{\partial Q_y}{\partial h}\right|_{h=H}\right), \tag{3.75}$$

with

$$\begin{aligned}
\left.\frac{\partial Q_y}{\partial \theta}\right|_{\theta=\theta_0} &= -Q_{f,0}\frac{\theta_{y,0}}{\theta_0^2} + Q'_{f,0}\frac{\theta_{y,0}}{\theta_0}, \\
\left.\frac{\partial Q_y}{\partial \theta_y}\right|_{\theta_y=\theta_{y,0}} &= Q_{f,0}\frac{1}{\theta_0}, \\
\left.\frac{\partial Q_y}{\partial h}\right|_{h=1} &= \mathrm{i}k\frac{1}{\theta_0^2}\left(\theta_{x,0}^2\frac{k_g}{\sqrt{\theta_0}}Q_{f,0} + \theta_{y,0}^2\frac{\theta_{cr}}{\mu_d}Q'_{f,0}\right),
\end{aligned} \tag{3.76}$$

and

$$\begin{aligned}
Q_{f,0} &\equiv \frac{30}{\pi\mu_d}(\theta_0 - \theta_{cr})(\sqrt{\theta_0} - 0.7\sqrt{\theta_{cr}}), \\
Q'_{f,0} &\equiv \left.\frac{\partial Q_f}{\partial \theta}\right|_{\theta=\theta_0} = \frac{15}{\pi\mu_d\sqrt{\theta_0}}\left(3\theta_0 - 1.4\sqrt{\theta_{cr}\theta_0} - \theta_{cr}\right).
\end{aligned} \tag{3.77}$$

Since the problem is uniform in the $x-$direction, $Q_{x,1}$ will vanish.

If the total flow is symmetrical in time, the bed forms do not migrate, hence $\Gamma_i = 0$. The growth rate Γ_r is determined for any value of the wavenumber k and the angle α, given any fixed combinations of the model parameters. The perturbation with the largest growth rate is called the fastest growing mode and is expected to dominate the solution after some time. The time evolution of the amplitude of the bed forms is described by $\exp(\Gamma_r t)$.

4 Design of Experiments

For the numerical implementation, the problem is made dimensionless. The dimensionless model has dimensionless input parameters. The latter are calculated from the dimensional input parameters, which are

- U_{da} depth-averaged tidal flow amplitude [m s^{-1}];
- ε_{da} eccentricity of the tidal ellipse described by the depth-averaged flow;
- α inclination of the long axis of the tidal ellipse described by the depth-averaged flow [^{o}];
- k wavenumber of the bed perturbation [m^{-1}];
- H total water depth [m];
- f Coriolis parameter [s^{-1}];
- ω_{M_2} the semi-diurnal M_2-tide frequency [s^{-1}];
- d uniform sediment grain size [m];
- c_v constant for the vertical eddy viscosity;
- k_g constant for the sediment transport due to bed slopes;
- μ_d friction coefficient of the sediment mixture;
- θ_{cr} critical Shields parameter for sediment movement.

In case of more than one tidal constituents, the model input also includes A, Φ and ω, which are respectively the amplitude, phase and frequency of all other harmonics that constitute the depth-averaged (basic state) currents.

Table 4.1 provides the default values of the input parameters. These values are representa-

U_{da}	ε_{da}	H	f	ω_{M_2}
0.6 m s^{-1}	0.4	40 m	$1.12 \cdot 10^{-4}$ s^{-1}	$1.4 \cdot 10^{-4}$ s^{-1}
d	c_v	k_g	μ_d	θ_{cr}
0.4 mm	$2.5 \cdot 10^{-3}$	0.55	0.6	0.05

Table 4.1: The default values of the input parameters

tive of the coastal area considered by Knaapen et al. (2001) and are also used by Blondeaux et al. (2009) as parameter values for which their model provides the growth of long bed waves.

In every model run, values of α in the range $[-90^o - 90^o]$ are tried, together with k in the range $[0, 2\pi \cdot 10^{-3}]$ (such that the wavelength of the smallest bed perturbations is 1 km). Also, the number of levels N in the hydrodynamic module must be set at the beginning of the run.

4.1 Linearization of Bed Shear Stress

The first research question involves examining the effect of the linearization of the bed shear stress, as is employed in this study, on the growth and spatial patterns of the fastest growing bed perturbations. To this aim, output of the one-level version of the present model is compared with that of Blondeaux et al. (2009), who used quadratic bed shear stress. The default values of the input variables (Table 4.1) are used for this model run (model run 1-1). The tidal flow of the basic state is restricted to the M_2-tide and since this flow is symmetrical in time, the bed forms will not migrate.

4.2 Changing Water Depth

Are the properties of tidal sand ridges and long bed waves sensitive to changing water depth? In order to answer this (second) research question, the one-level model is ($N = 1$) is used. A basic state tidal flow is considered that describes a rectilinear tidal flow and consists of a single tidal constituent (the M_2-tide). While implementing a wide range of depths H for the model runs, the pressure gradient forces in Eq. 3.32 is kept fixed. These fixed pressure gradient forces (P_x, P_y) follow from the basic state in a first run (model run 2-1).

In model run 2-1, the input parameter values are as in Table 4.1, except for $U_{da} = 1$ m s^{-1} and $\varepsilon_{da} = 0$. This gives (using Eq. 3.27) $\gamma_1 = 1.42 \cdot 10^{-3}$ m s^{-1}. Using Eq. 3.48-3.51 with $N = 1$, the complex amplitudes of the fixed pressure gradient forces are thus

$$\begin{aligned} P_x &= \omega_{\mathrm{M}_2} \cos(\alpha) \cos(\omega_{\mathrm{M}_2} t) + [\gamma_1 / H \cos(\alpha) - f \sin(\alpha)] \sin(\omega_{\mathrm{M}_2} t) = \\ &= \Re\{\hat{p}_x e^{-\mathrm{i}\omega_{\mathrm{M}_2} t}\}, \\ P_y &= \omega_{\mathrm{M}_2} \sin(\alpha) \cos(\omega_{\mathrm{M}_2} t) + [\gamma_1 / H \sin(\alpha) + f \cos(\alpha)] \sin(\omega_{\mathrm{M}_2} t) = \\ &= \Re\{\hat{p}_y e^{-\mathrm{i}\omega_{\mathrm{M}_2} t}\}, \end{aligned} \tag{4.2}$$

with

$$\begin{aligned} \hat{p}_x &= 1.4 \cdot 10^{-4} \cos(\alpha) + \mathrm{i}[3.55 \cdot 10^{-5} \cos(\alpha) - 1.12 \cdot 10^{-4} \sin(\alpha)], \\ \hat{p}_y &= 1.4 \cdot 10^{-4} \sin(\alpha) + \mathrm{i}[3.55 \cdot 10^{-5} \sin(\alpha) + 1.12 \cdot 10^{-4} \cos(\alpha)]. \end{aligned} \tag{4.3}$$

The parameters that are varied in the other model runs are H and U_{da}. In these model runs, the local water depth H is imposed and the amplitude of the depth-averaged tidal flow velocity U_{da} follows from the constraint that the pressure gradient forces are fixed. An overview the imposed values of H and the corresponding model runs is in Table 4.2 (all other input parameters are as in model run 2-1).

model run 2-1	model run 2-2a	model run 2-2b
$H = 40$ m	$H = 30$ m	$H = 24$ m

Table 4.2: The different values of H in the model runs used for research question 2. For other input parameter values, see text.

The procedure to compute the value of U_{da} is shown here. For any value of H, the complex amplitudes $\hat{u}$ and $\hat{v}$ of the basic state are obtained from solving

$$\begin{pmatrix} -\mathrm{i}\omega_{\mathrm{M}_2} + \gamma_1/H & -f \\ f & -\mathrm{i}\omega_{\mathrm{M}_2} + \gamma_1/H \end{pmatrix} \begin{pmatrix} \hat{u} \\ \hat{v} \end{pmatrix} = \begin{pmatrix} \hat{p}_x \\ \hat{p}_y \end{pmatrix}. \tag{4.4}$$

However, γ_1 depends on U_{da} as

$$\gamma_1 = \frac{8}{3\pi} \frac{1}{C^2} U_{da}, \tag{4.5}$$

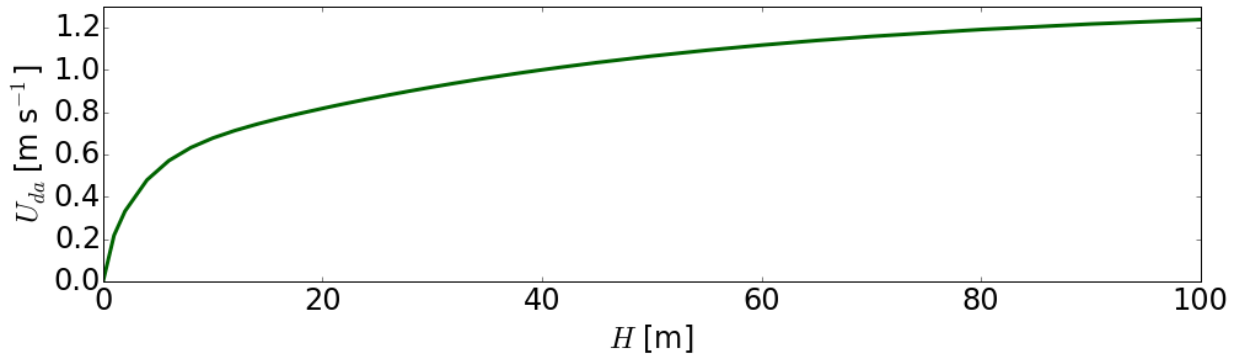

Figure 4.1: The amplitude U_{da} of the depth-averaged tidal flow as a function of local water depth H, obtained from the iterative process. The other input parameters are as in Table 4.1.

and U_{da} is at this point unknown. An iterative process is used to obtain a value of U_{da} and thus of γ_1. The first guess value ($j = 1$) is for $U_{da}^{(1)} = 1$ m s^{-1}. Substitution of the corresponding value of γ_1 in Eq. 4.4 results in values of $\hat{u}$ and $\hat{v}$. In the next iteration the following value of U_{da} is used:

$$U_{da}^{(j+1)} = \sqrt{|\hat{u}|^2 + |\hat{v}|^2}. \tag{4.6}$$

If two subsequent values of U_{da} are within a certain tolerance $\delta = 10^{-6}$ m s^{-1}, the iterative procedure is finished, i.e. if

$$|U_{da}^{(j+1)} - U_{da}^{(j)}| < \delta. \tag{4.7}$$

In Fig. 4.1, the resulting U_{da} is plotted as a function of H.

4.3 Vertical Structure of the Tidal Currents

4.3.1 Orientation of Long Bed Waves

Research question 3a was "Can the vertical structure of the tidal currents explain the difference between modelled and observed orientation of long bed waves?". To address this research question, model run 3a is carried out. In this run the default values for the input parameters (Table 4.1) are used and the number of levels N is varied. Model run 3a with $N = 1$ is the same as model run 1-1.

The output of the one-level model ($N = 1$) is compared with the that of the multilevel model ($N = 2, \dots$). The initial characteristics of the bed forms (orientation, wavelength and growth rate) are examined as a function of N. By increasing the value of N, the vertical structure of the tidal currents is increased. In this way, the effect of the vertical structure of the tidal currents on the orientation of long bed waves is examined.

4.3.2 Formation of Long Bed Waves

Blondeaux et al. (2009) identified that, in order for long bed waves to exist, it was necessary that $\varepsilon_{da} > 0.2$ and that U_{da} is close to the critical value for sediment transport. In fact, the growth of long bed waves was found when the tidal conditions are close to those presented in Table 4.1. It is tested if Ekman veering can also play a role in the formation of long bed waves. If this is the case the question arises whether the conditions as postulated by Blondeaux et al. (2009) are still necessary if Ekman veering is included? In fact, this is research question 3b. The default values (Table 4.1) for the input parameters are varied to examine this. The model runs that are conducted are in Table 4.3.

Model Run	Non-default input parameters	
3b-1	$\varepsilon_{da} = 0$	$N = 1, \dots$
3b-2	$U_{da} = 0.9$ m s^{-1}	"
3b-3	$U_{da} = 0.9$ m s^{-1}, $\varepsilon_{da} = 0$	"

Table 4.3: The model runs to address research question 3b. Here, N is the number of levels imposed to the model. The other input parameters are as in Table 4.1.

In model run 3b-1, the eccentricity of the depth-averaged tidal ellipse is set to zero. The tidal strength is increased to $U_{da} = 0.9$ m s^{-1} in model run 3b-2 and 3b-3. In model run 3b-3, this is combined with $\varepsilon_{da} = 0$. In this way, it is tested if long bed waves are also allowed to form when the tidal currents are stronger and when the eccentricity of the depth-averaged tidal ellipse is removed.

4.4 Spring-Neap Cycle

The last (fourth) research question (How does the spring-neap cycle affect the properties of the bed forms?) is addressed as follows. So far, the tidal flow is restricted to the M_2-tide (single harmonic). Here, the model runs 3a, 3b-1, 3b-2 and 3b-3 are repeated with inclusion of the spring-neap cycle. These model runs will be referred to as model runs 4-1, 4-2, 4-3 and 4-4, respectively (see Table 4.4). Other constituents, such as the diurnal K_1- and O_1tide are not considered.

Model Run	Non-default input parameters	
4-1	none	$N = 1, \ldots$
4-2	$\varepsilon_{da} = 0$	”
4-3	$U_{da} = 0.9$ m s^{-1}	”
4-4	$U_{da} = 0.9$ m s^{-1}, $\varepsilon_{da} = 0$	”

Table 4.4: The model runs to address research question 4. Here, N is the number of levels imposed to the model. The other input parameters are as in Table 4.1.

With the spring-neap cycle, the total depth-averaged tidal flow amplitude U_{da} is divided into U_{M_2} and U_{S_2}, which are the depth-averaged flow amplitudes of the M_2- and S_2-tide, respectively, i.e.,

$$U_{da} = U_{\mathrm{M}_2} + U_{\mathrm{S}_2}. \tag{4.8}$$

Equation 4.8 is such that U_{da} is the maximum depth-averaged flow velocity during the spring-neap cycle, which is reached during the spring phase when sun, moon, and earth are more or less aligned and the tidal force due to the sun reinforces that due to the moon.

Models runs are done with a fixed ratio between the S_2- and the dominant M_2-tide. A typical value in the North Sea for this ratio is chosen. In model runs 4-1 to 4-4, following Pugh (1996), the ratio is set at

$$\frac{U_{\mathrm{S}_2}}{U_{\mathrm{M}_2}} = 0.3. \tag{4.9}$$

It must be noted that the orientation of the long axis of both constituents are identical.

5 Results

For convenience, the wavenumber k is scaled with the tidal excursion length of the default run (Table 4.1). The results in this chapter are presented with usage of the scaled wavenumber

$$K \equiv k\frac{U_{da}}{\omega_{\mathrm{M_2}}} = \frac{2\pi U_{da}}{\lambda\omega_{\mathrm{M_2}}} \quad \rightarrow \quad \lambda \simeq \frac{26928 \text{ m}}{K}. \tag{5.1}$$

5.1 Linearization of Bed Shear Stress

In model run 1-1, the input parameters have their default values (Table 4.1). Figure 5.1a is a colour plot of growth rate Γ_r of bed perturbations as a function of α and K for this model run. The outcome of the model of Blondeaux et al. (2009) for the same values of the input

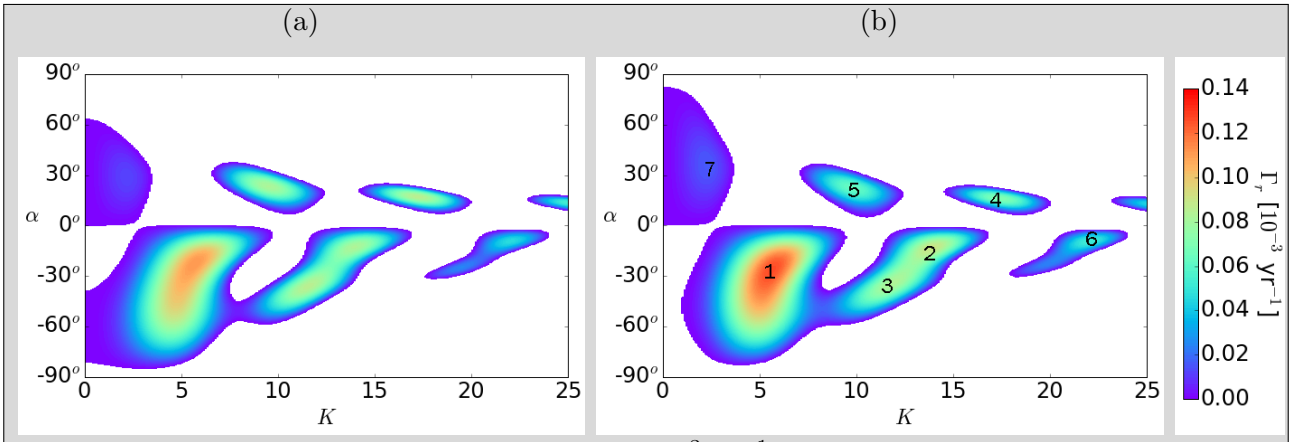

Figure 5.1: Colour plot of the growth rate Γ_r $[10^{-3}$ yr$^{-1}]$ of the bed perturbations as function of scaled wavenumber K and angle α between crests and the long axis of the tidal ellipse for default values for input parameters (Table 4.1). Only positive values are shown.
(a) model run 1-1 (linearized bed shear stress);
(b) Blondeaux et al. (2009) (quadratic bed shear stress).

Mode	Fig. 5.1a			Fig. 5.1b		
	Γ_r [10^{-3} yr^{-1}]	λ [km]	α [^{o}]	Γ_r [10^{-3} yr^{-1}]	λ [km]	α [^{o}]
1	0.1115	4.7	-22.5	0.1265	4.8	-26.5
2	0.0824	1.9	-13	0.09	1.9	-13
3	0.0857	2.3	-36	0.082	2.3	-34
4	0.0856	1.6	17	0.0705	1.5	16
5	0.0822	2.8	23.5	0.0631	2.7	22.5
6	0.0461	1.2	-9.5	0.0524	1.2	-9.5
7	0.0121	12.2	29	0.0157	11.7	35.5

Table 5.1: Characteristics of all relative maxima in Fig. 5.1, ordered by growth rate.

parameters is in Fig. 5.1b.

Table 5.1 gives an overview of the characteristics of all relative maxima in Fig. 5.1. The fastest growing mode, resembling tidal sand ridges, rotates cyclonically (counterclockwise) by ~ 4 degrees when the bed shear stress is linearized. The geometrical characteristics (λ, α) of the other relative maxima do not change significantly. The growth rates for most modes with $\alpha < 0^o$ ($\alpha > 0^o$) are slightly smaller (larger) for the case that the bed shear stress is linearized.

5.2 Changing Water Depth

In this section, only tidal sand ridges are considered. Long bed waves only form when the maximum tidal flow velocity U_{da} is just above the threshold value for sediment transport. When local water depth H decreases, so does U_{da} and below a certain value, no bed forms form. Increasing H only enhances the growth of tidal sand ridges and long bed waves are then less likely to form.

Figure 5.2 shows a colour plot of the growth rate Γ_r as function of K and α for model run 2−1 ($H = 40$ m). The fastest growing mode corresponds to tidal sand banks with wavelength of 8.8 km and its crests are cyclonically rotated (angle of 37.7^o) with respect to the rectilinear tidal flow. The e-folding time of this mode is 612 years.

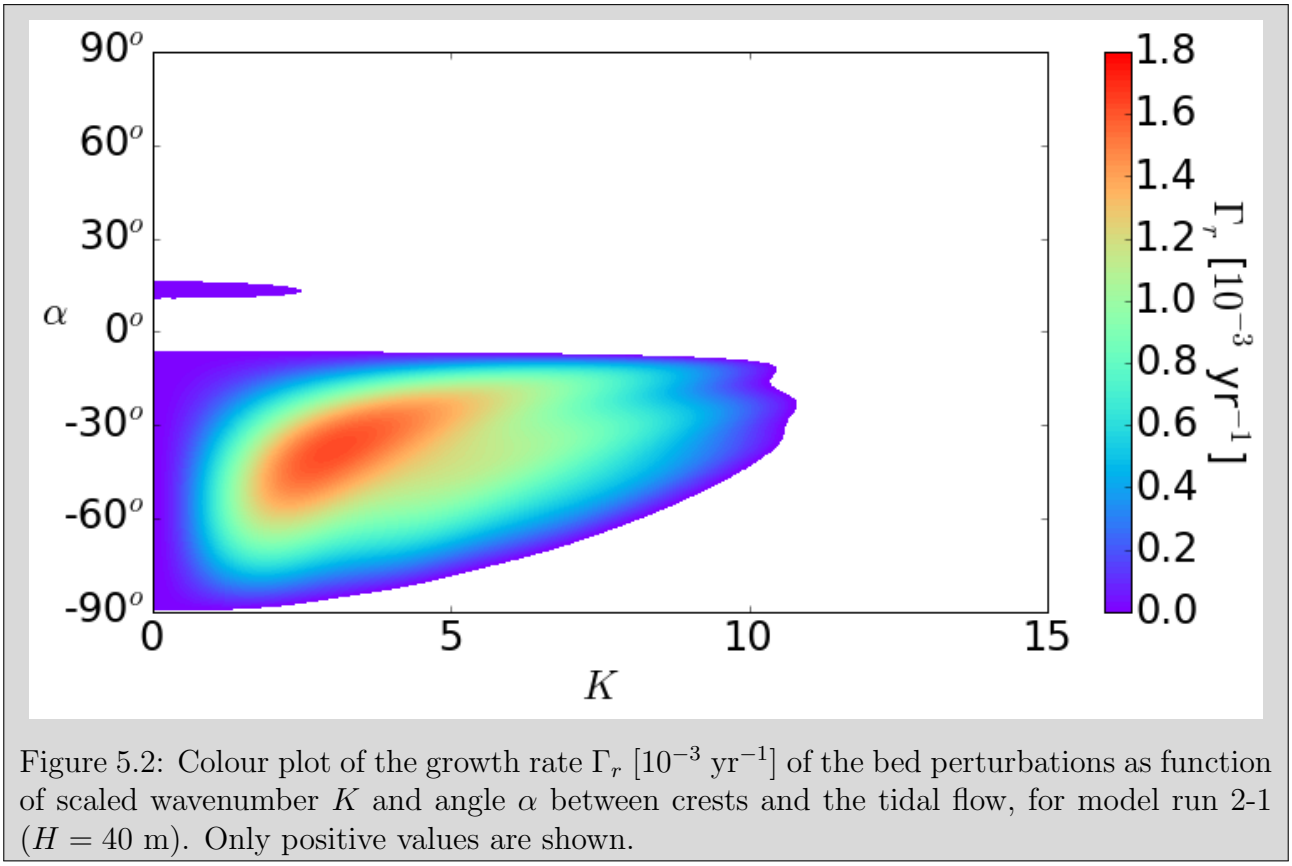

Figure 5.2: Colour plot of the growth rate Γ_r [10^{-3} yr^{-1}] of the bed perturbations as function of scaled wavenumber K and angle α between crests and the tidal flow, for model run 2-1 ($H = 40$ m). Only positive values are shown.

Figure 5.3 shows the same plot for model run 2-2a and 2-2b where $H = 30$ m and $H = 24$ m, respectively. For model run 2-2a, the fastest growing mode has crests which are cyclonically rotated with respect to the direction of the tidal current ($\alpha = -33.5^o$) and a crest-to-crest distance of about 6 km. Another relative maximum, with a smaller growth rate, is seen in Fig. 5.3a, viz. for $K = 7.1$ ($\lambda = 3.8$ km) and $\alpha = 13.5^o$. This mode is called the second mode.

The maximum growth rate in Fig. 5.3a is slightly smaller than the one in Fig. 5.2. Now the e-folding time of the fastest growing mode is 702 yr. Qualitatively, the second growing mode

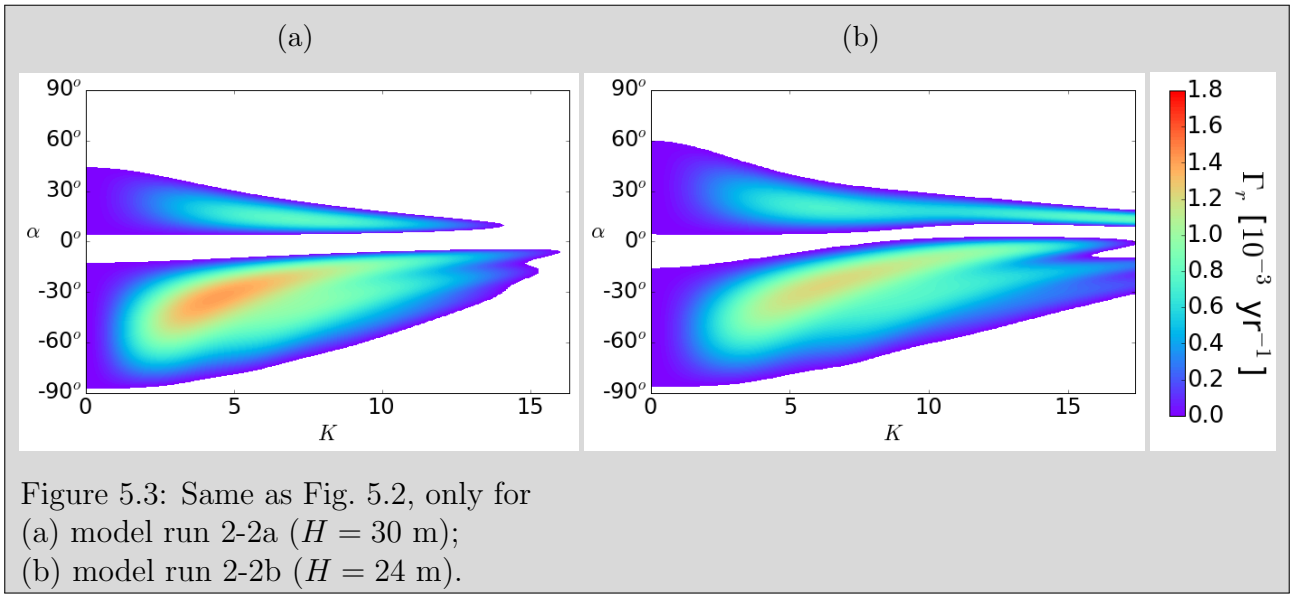

Figure 5.3: Same as Fig. 5.2, only for
(a) model run 2-2a ($H = 30$ m);
(b) model run 2-2b ($H = 24$ m).

is also found for model run 2-2b. Here, again, the growth rate of the fastest growing mode is smaller than for $H = 30$ m (e-folding time of 217 yr).

In Fig. 5.3b, a third growing mode appears, which has small wavelength (~ 1.6 km) and is anticyclonically rotated with respect to the direction of the tidal current ($\alpha = 14^o$). This mode is only found when the threshold velocity value for erosion is included and when the maximum tidal flow velocity is just above this value. The inference is that this mode can be linked to the anticyclonically oriented long bed waves.

The wavelength, orientation and growth rates of the three modes as a function of local water depth is shown in Fig. 5.4. Not only the maximum growth rate changes with water depth, so do the orientation and crest-to-crest difference of the fastest growing mode (shown in blue). The angle of the crests with the tidal current increases from -37.7^o to -23.6^o when the local water depth decreases from 40 m to 22 m. This qualitatively agrees with results found by Hulscher (1996), who found that if the Coriolis force is dominant (relatively larger local water depths), the angle will be larger and if friction dominates (smaller values of H), the angle will be smaller.

Also, the crest-to-crest-distance decreases from 8.8 km to 4 km when the local water depth decreases from 40 m to 22 m. Qualitatively, this agrees to the findings of Huthnance (1982). According to Huthnance's model, tidal sand ridges mainly develop with wavelengths that are 250 times the local water depth. Similar trends are seen for $H > 40$ m.

For most values of local water depth H, the fastest growing mode resembles tidal sand ridges with crests which are cyclonically rotated with respect to the direction of the tidal current ($\alpha < 0^o$). However, for shallow seas (local water depth below ~ 21m), the third mode has the largest growth rate. The growth rate of the fastest growing mode in the domain $\alpha < 0^o$ decreases monotonically with decreasing water depth. The second (third) growing mode has its maximum growing rate around $H \sim 28$ m ($H \sim 18$m). For $H < 17.5$m, the maximum flow velocity is below the critical value for sediment transport and $\Gamma_r = 0$.

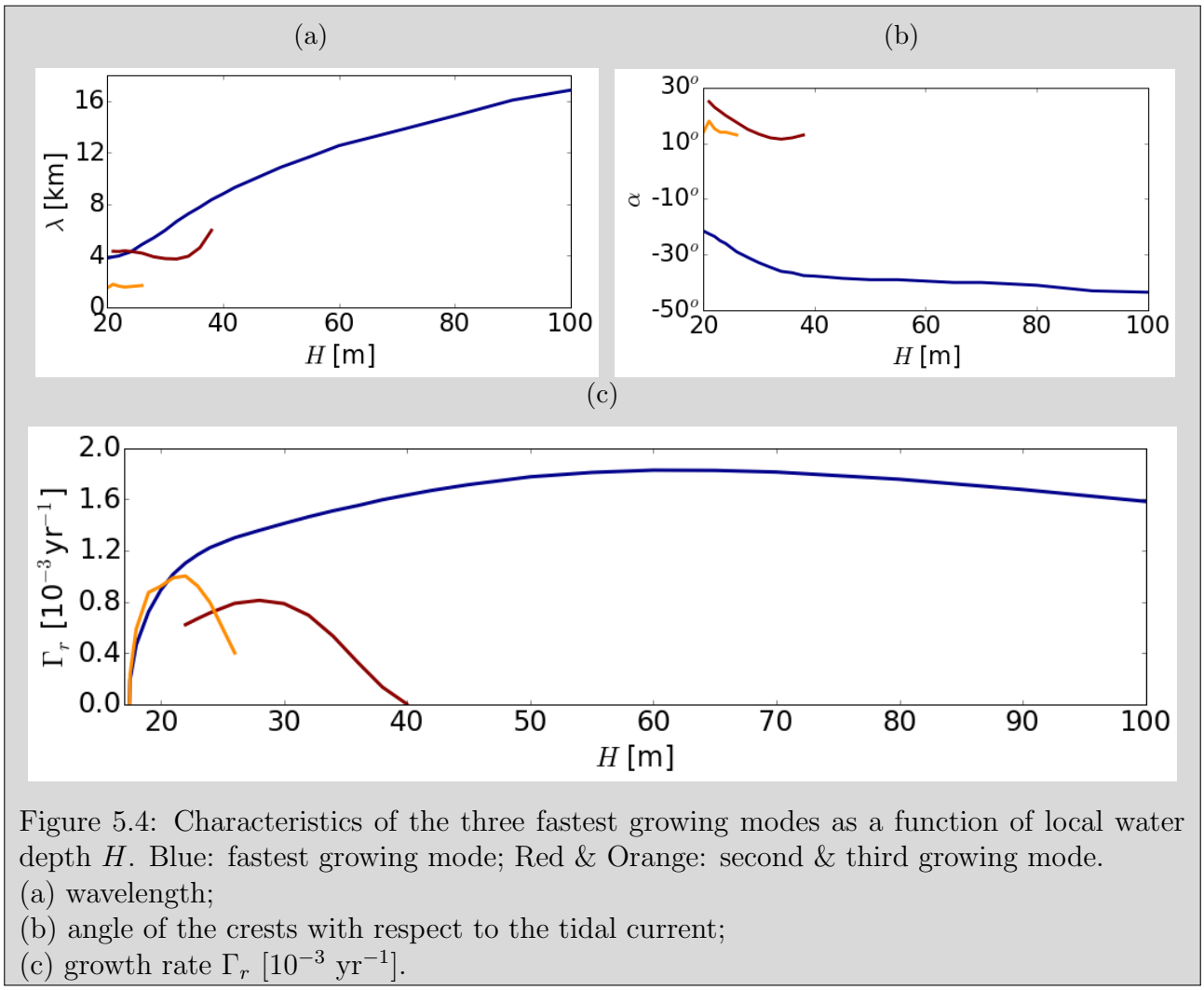

Figure 5.4: Characteristics of the three fastest growing modes as a function of local water depth H. Blue: fastest growing mode; Red & Orange: second & third growing mode.
(a) wavelength;
(b) angle of the crests with respect to the tidal current;
(c) growth rate Γ_r [10^{-3} yr^{-1}].

When the local water depth exceeds $\sim$ 40 m, only one growing mode remains: the fastest growing mode. The maximum growth rate is found for $H \sim 60$ m. Larger values for H reduce the growth rate (Eq. 3.68) and for smaller values for H smaller tidal flow amplitude U_{da} are found, which also reduces the growth rate. Even though the amplitude of the depth-averaged tidal flow increases for larger water depths (see Fig. 4.1), the growth rate decreases. The tidal current does not reach the bottom of deeper seas, which explains why tidal sand ridges are only formed in shallow seas.

5.3 Vertical Structure of the Tidal Currents

5.3.1 Orientation of Long Bed Waves

In model run 3a, the input parameters have their default values (Table 4.1). A colour plot of the growth rates computed by the one-level model ($N = 1$) is shown in Fig. 5.1a. The fastest growing mode resembles tidal sand ridges with $\alpha = -22.5^o$, $\lambda = 4.7$ km and e-folding timescale of $\sim$ 9000 years. Four other relative maxima can be identified, viz. for λ equal to about 1.6 km, 1.9 km, 2.3 km and 2.8 km and α equal to about 17^o, -13^o, -36^o and 23.5^o, respectively. Blondeaux et al. (2009) linked these modes to long bed waves, despite the discrepancy between the orientation of the modelled bed forms and the observed values.

By increasing the number of levels N, the vertical structure of the tidal flow is enhanced. Figure 5.5 presents the wavelength and orientation of the modes as a function of N. At $N = 2$, the two modes in Fig. 5.1a that could be linked to cyclonic turned long bed waves (shown in orange) have merged.

Figure 5.6 shows the wavelength, orientation and growth rate of the modes as function of N. Increasing the vertical structure of the tidal currents has little effect on the wavelength. The wavelength of the mode that resembles tidal sand ridges (blue) decreases from 4.7 km to

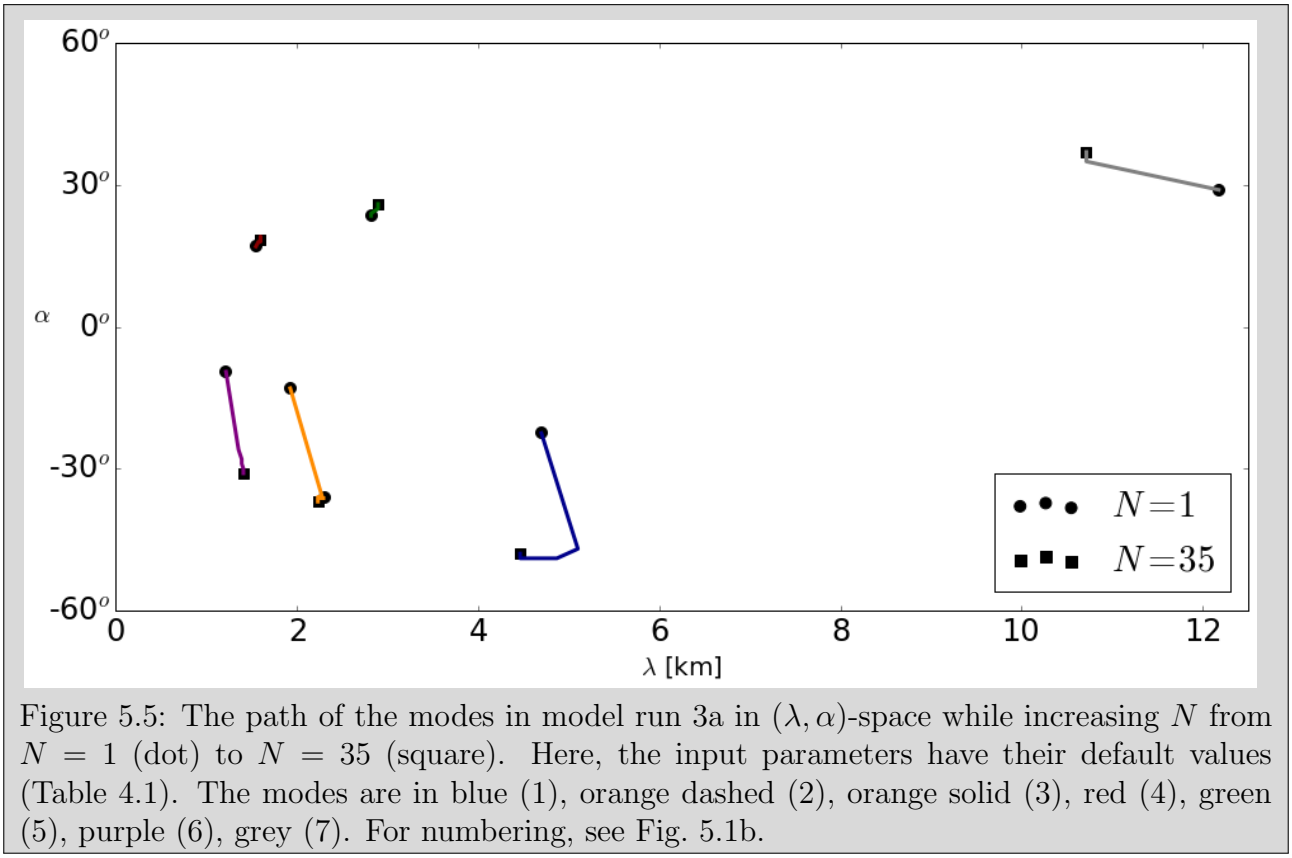

Figure 5.5: The path of the modes in model run 3a in (λ, α)-space while increasing N from $N = 1$ (dot) to $N = 35$ (square). Here, the input parameters have their default values (Table 4.1). The modes are in blue (1), orange dashed (2), orange solid (3), red (4), green (5), purple (6), grey (7). For numbering, see Fig. 5.1b.

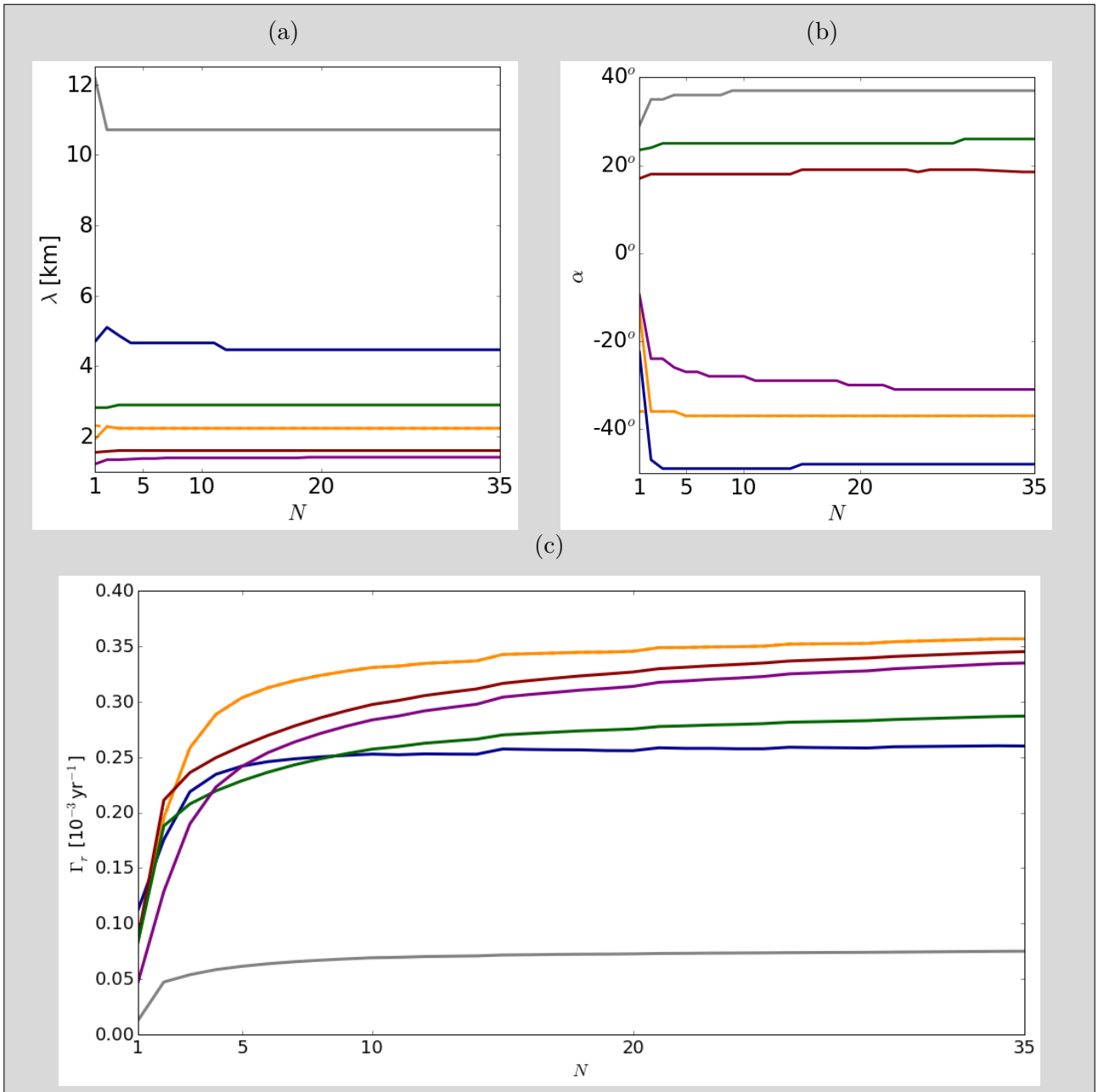

Figure 5.6: Characteristics of the modes in model run 3a as a function of local water depth H. The modes are in blue (1), orange dashed (2), orange solid (3), red (4), green (5), purple (6), grey (7). For numbering, see Fig. 5.1b.
(a) wavelength λ [km];
(b) angle of the tidal current with respect to the crests α [^{o}];
(c) growth rate Γ_r [10^{-3} yr^{-1}].

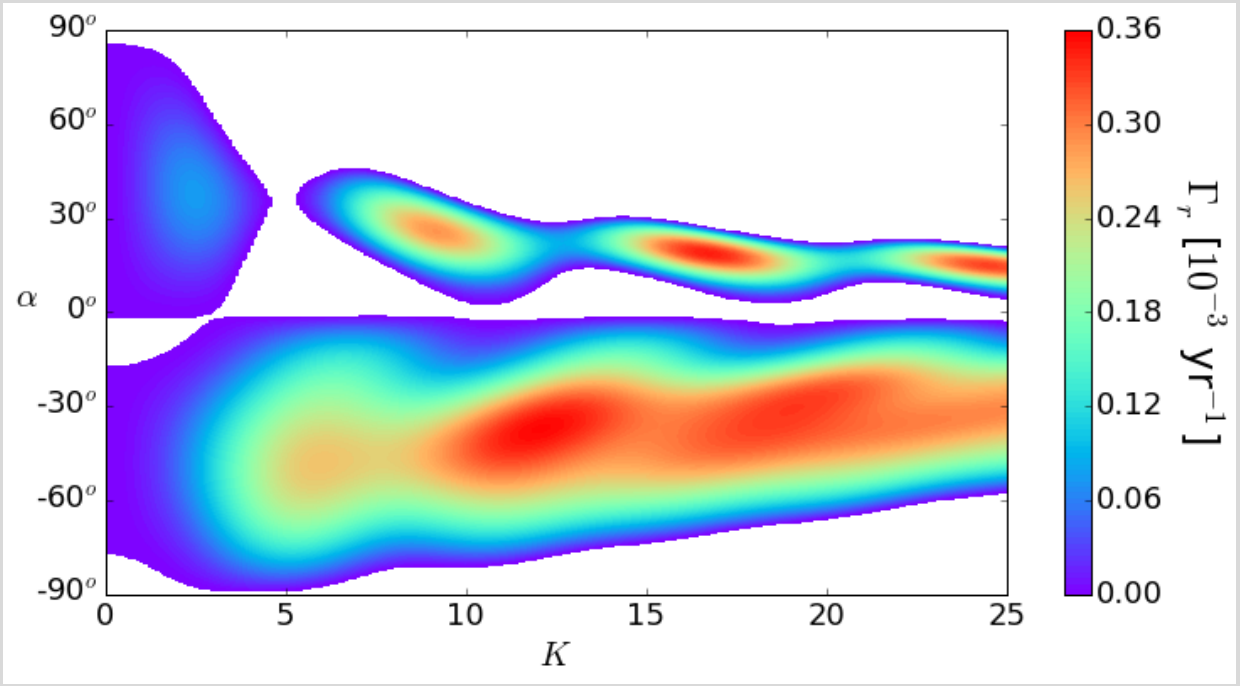

Figure 5.7: Colour plot of the growth rate Γ_r [10^{-3} yr^{-1}] of the bed perturbations as function of scaled wavenumber K and angle α between crests and the tidal flow for default values for input parameters (Table 4.1): model run 3a with $N = 35$. Only positive values are shown.

4.4 km when the number of levels is increases from 1 to 35.

The angle between the crests of the modes and the long axis of the tidal ellipse increases with increasing N. However, this effect is much greater for cyclonically ($\alpha < 0^o$) than for anticyclonically ($\alpha > 0^o$) oriented modes. The difference in angle for the former is between 21.5^o and 25.5^o. For the latter, this is between 0^o and 8^o.

When one increases the number of levels, the model provides increasing growth rates. While the geometrical characteristics of the modes only depend on the number of levels for small values of N (after which they converge), more levels are needed for the growth rates to converge. In this case, the growth rates have reached their 'equilibrium' value around $N \sim 25$.

For model run 3a with $N = 35$, when the wavelength, orientation and growth rates of the

Mode	$\Gamma_r[10^{-3}\text{yr}^{-1}]$	λ [km]	$\alpha[^o]$
1	0.2601	4.5	-48
2	0.3568	2.2	-37
3	0.3453	1.6	19
4	0.3350	1.4	-31
5	0.2871	2.9	26
6	0.0749	10.7	37.5

Table 5.2: Characteristics of all relative maxima in Fig. 5.7.

modes are converged, a colour plot of the growth rates as a function of K and α is in Fig. 5.7. Comparison with the output of model run 3a with $N = 1$ (Fig. 5.1a) reveals that the amount of bed perturbations with positive growth rates has increased, mainly for large values of K (small wavelengths). Table 5.2 presents an overview of the characteristics of the modes.

5.3.2 Formation of Long Bed Waves

In model run 3b-1, the eccentricity of the depth-averaged tidal ellipse is removed, while the other input parameters have their default values (Table 4.1). A colour plot of the growth rates with $N = 1$ and $N = 35$ is in Fig. 5.8a and Fig. 5.8b, respectively. How the characteristics of the modes change with increasing N is in Fig. 5.9.

The one-level model output does not show the presence of long bed waves. Only one mode is found ($\lambda = 4.9$ km, $\alpha = -39^o$), which resembles tidal sand ridges. When the number of levels N is increased, two other relative maxima appear: the second and third mode.

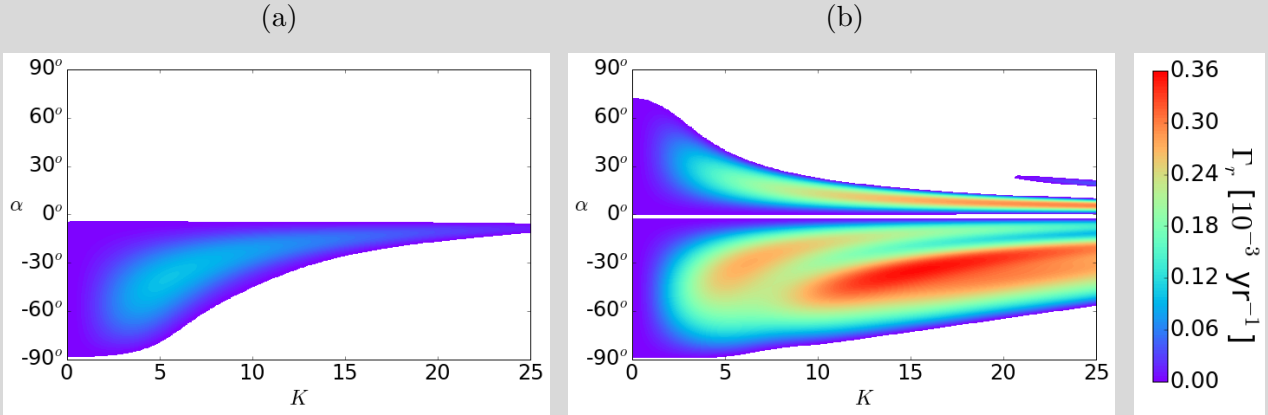

Figure 5.8: Colour plot of the growth rate Γ_r [10^{-3} yr^{-1}] of the bed perturbations as function of scaled wavenumber K and angle α between crests and the tidal flow for default values for input parameters (Table 4.1) except $\varepsilon_{da} = 0$. Only positive values are shown.
(a) model run 3b-1 with $N = 1$;
(b) model run 3b-1 with $N = 35$.

The second mode, with $\lambda = 1.5$ km and $\alpha = 8^o$, is already part of the model output when $N = 2$ and the geometrical characteristics do not change with increasing N. This mode could be linked to the anticyclonically oriented long bed waves. With $N = 3$, the third mode appears. This mode, of which the geometrical characteristics converge to $\lambda = 1.7$ km and $\alpha = -37^o$, resembles the cyclonically oriented long bed waves.

While increasing the number of levels, the orientation of the tidal sand ridges changes (blue line in Fig. 5.9). The angle between crests and tides is 37^o for $N = 1$ and converges to about 30^o. For $N = 35$, the tidal conditions are such that tidal sand ridges and both types of long bed waves are allowed to grow. With an $e-$folding timescale of about 2800 years, the third mode is the fastest growing mode.

So far, the model runs were done with the default value for the tidal strength ($U_{da} = 0.6$ m s^{-1}), which is close to the critical value for sediment transport. In model run 3b-2 and 3b-3, the tidal strength is increased to 0.9 m s^{-1}. In model run 3b-2 and 3b-3, the eccentricity ε_{da} of the depth-averaged tidal ellipse is 0.4 and 0, respectively. Figure 5.10 presents a colour plot of the growth rates for these models runs with $N = 1$ and $N = 20$.

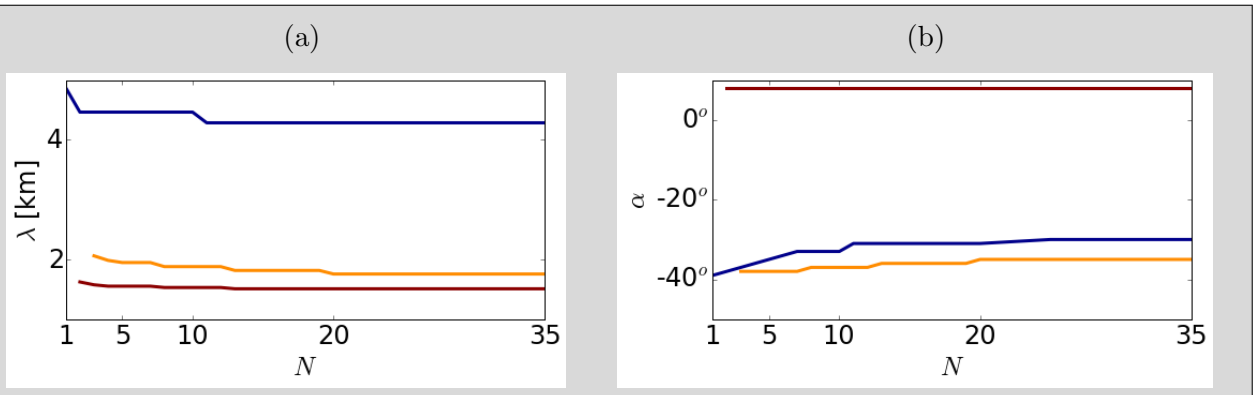

Figure 5.9: Geometrical characteristics of the modes in model run 3b-1 as a function of local water depth H. The modes are in blue (1), red (2), orange (3).
(a) wavelength;
(b) angle of the tidal current with respect to the crests.

As for model run 3b-2: in the output of the one-level model, only one mode with significant growth rate is present, which has wavelength (8.1 km) and orientation ($\alpha = -39^o$) close to that of tidal sand ridges. The output of the multilevel model reveals several modes, all with comparable growth rates ($e-$folding timescales between about 350 and 400 years) and orientation (α between -51^o and -48^o). The wavelengths of these modes range from 2.2 to 18 km.

Some of these modes, especially those with $K = 4.5$ ($\lambda = 5.9$ km) and $K = 7.17$ ($\lambda = 3.7$ km) resemble tidal sand ridges. The mode with the largest value of K has a wavelength of about 2.2 km. The geometrical characteristics are similar to those of cyclonically rotated long bed waves. No anticyclonically rotated modes are found.

For model run 3b-3, the output of the one-level model only shows the mode that resembles tidal sand ridges ($\lambda = 8.0$ km, $\alpha = -39^o$). Increasing the number of levels decreases the wavelength of this mode greatly. For $N = 20$, the wavelength has converged to around 2.6 km. This mode represents a large area of bed perturbations with positive growth rate. Also, one anticyclonically rotated mode can be seen. This mode, with a smaller growth rate than the first mode has wavelength of about 4.3 km and α of about 14^o.

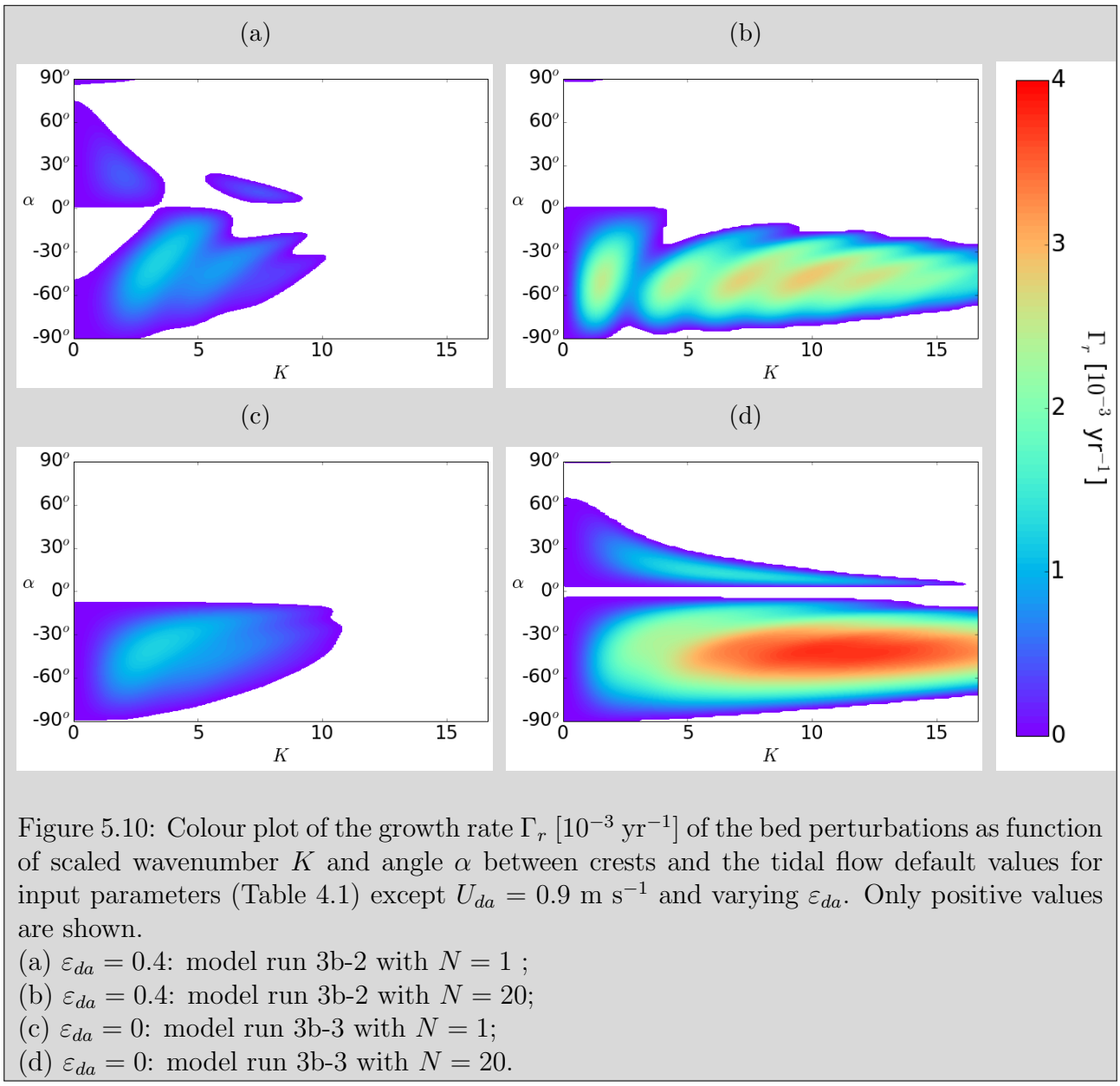

Figure 5.10: Colour plot of the growth rate Γ_r $[10^{-3}\ \mathrm{yr}^{-1}]$ of the bed perturbations as function of scaled wavenumber K and angle α between crests and the tidal flow default values for input parameters (Table 4.1) except $U_{da} = 0.9$ m s^{-1} and varying ε_{da}. Only positive values are shown.
(a) $\varepsilon_{da} = 0.4$: model run 3b-2 with $N = 1$;
(b) $\varepsilon_{da} = 0.4$: model run 3b-2 with $N = 20$;
(c) $\varepsilon_{da} = 0$: model run 3b-3 with $N = 1$;
(d) $\varepsilon_{da} = 0$: model run 3b-3 with $N = 20$.

5.4 Spring-Neap Cycle

Two situations are considered. First, the effect of the spring-neap cycle on the formation of long bed waves is examined. Subsequently, it is examined if the formation the tidal sand ridges is affected by the spring-neap cycle.

As for the formation of long bed waves, model runs 4-1 and 4-2 are done. The effect of the spring-neap cycle is examined by setting the ratio U_{S_2}/U_{M_2} to 0.3 while fixing $U_{da} = U_{S_2} + U_{M_2}$. For model run 4-1, the input parameter values are as in Table 4.1. A colour plot of the growth rates for this model run with $N = 35$ is shown in Fig. 5.11a. In this case, the wavelength and orientation of the modes are the same as those of the modes for the the single harmonic in Fig. 5.7, i.e. the spring-neap cycle has no effect on the wavelengths and orientations of the modes.

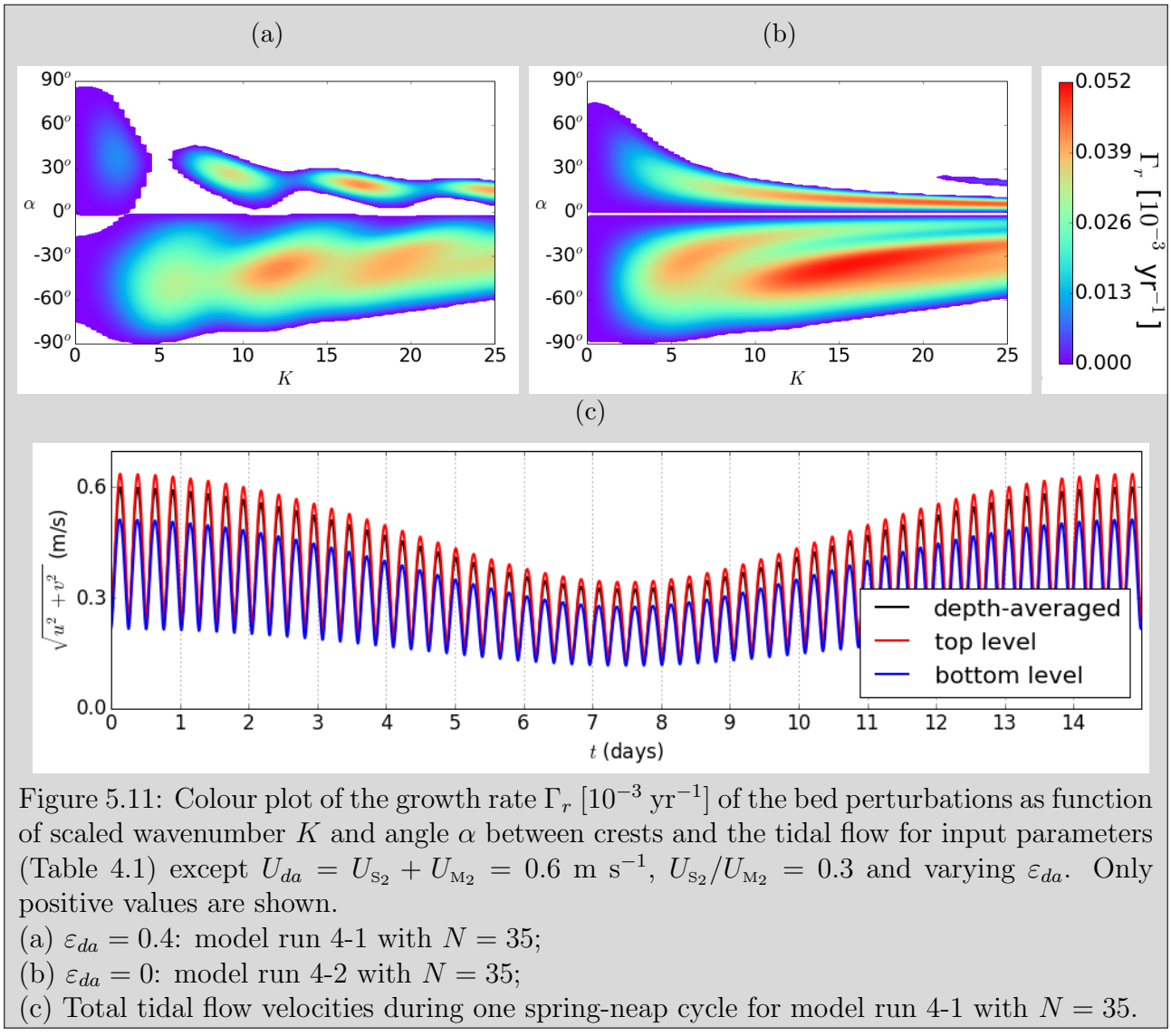

Figure 5.11: Colour plot of the growth rate Γ_r [10^{-3} yr^{-1}] of the bed perturbations as function of scaled wavenumber K and angle α between crests and the tidal flow for input parameters (Table 4.1) except $U_{da} = U_{S_2} + U_{M_2} = 0.6$ m s^{-1}, $U_{S_2}/U_{M_2} = 0.3$ and varying ε_{da}. Only positive values are shown.
(a) $\varepsilon_{da} = 0.4$: model run 4-1 with $N = 35$;
(b) $\varepsilon_{da} = 0$: model run 4-2 with $N = 35$;
(c) Total tidal flow velocities during one spring-neap cycle for model run 4-1 with $N = 35$.

However, the $e-$folding time of the fastest growing mode in Fig. 5.11a is more than 19000 years, which is much longer than the 2800 years for the single harmonic. The tidal flow velocity is below the threshold value for erosion during most part of the spring-neap cycle. Including the spring-neap cycle thus affects the growth rates.

In model run 4-2 the eccentricity of the depth-averaged tidal ellipse is removed, i.e., $\varepsilon_{da} = 0$, other input parameter have their default values (Table 4.1). The colour plot of the growth rates for this model run with $N = 35$ is shown in Fig. 5.11b. Again, the wavelengths and orientations of the modes do not differ from those of the modes found for the single harmonic (Fig. 5.8b), but their growth rates are smaller.

The model runs 4-3 and 4-4 are done to examine the effect of the spring-neap cycle on the effect of the tidal sand ridges. In model run 4-3, the tides are stronger, i.e. $U_{da} = 0.9$ m s^{-1} where other input parameter have their default values (Table 4.1). In model run 4-4, $U_{da} = 0.9$ m s^{-1} and $\varepsilon_{da} = 0$ where other input parameter have their default values (Table 4.1). Figure 5.12 presents a colour plot of the growth rates of the bed perturbations for model runs 4-3 and 4-4 with $N = 20$.

Since the tidal flow velocity is above the threshold value for sediment movement during a larger part of the spring-neap cycle, the growth rates decrease less than for model runs 4-1 and 4-2. For the rectilinear tide , the wavelengths and orientations of the two modes are not different than those of the modes found for the single harmonic (Fig. 5.10d).

However, the spring-neap cycle has an effect on the modelled growth rates for the elliptical tide. The growth rates for the single harmonic are in Fig. 5.10b. The different distinguishable modes with $\alpha \sim -48^o$ merge into one mode with $\lambda = 2.3$ km and $\alpha = -44^o$.

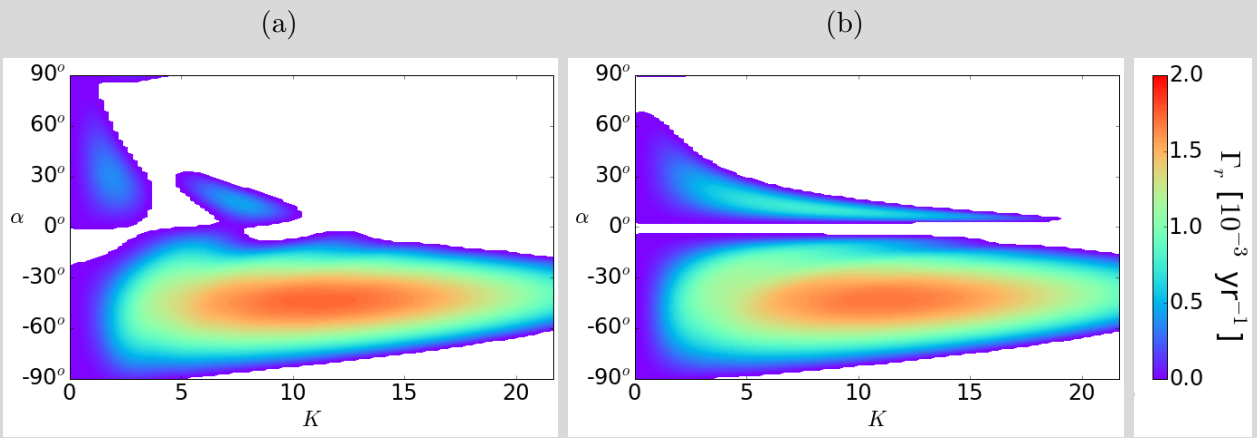

Figure 5.12: Colour plot of the growth rate Γ_r [10^{-3} yr^{-1}] of the bed perturbations as function of scaled wavenumber K and angle α between crests and the tidal flow for input parameters (Table 4.1) except $U_{da} = U_{S_2} + U_{M_2} = 0.9$ m s^{-1}, $U_{S_2}/U_{M_2} = 0.3$ and varying ε_{da}. Only positive values are shown.
(a) $\varepsilon_{da} = 0.4$: model run 4-3 with $N = 20$;
(b) $\varepsilon_{da} = 0$: model run 4-4 with $N = 20$.

6 Discussion

In this chapter is the discussion of the results. First, some remarkable elements of the results are discussed. Also, a physical interpretation of these results is given. Subsequently, the sensitivity of the results is tested for different values of the vertical eddy viscosity. Also, some model limitations are presented.

6.1 Some Remarkable Elements of the Results

In the case of strong tidal currents, as in Fig. 5.10, the mechanism that gives rise to the growth of the bed forms is well known. As discussed in section 2.2.1, the interaction of ridges and the oscillatory tidal current generates anticyclonic residual circulation. When the ridges are cyclonically rotated with respect to major axis of the tidal ellipse, the residual circulation causes sediment to be deposited at the crests and the amplitude of the ridges increases. In contrast, for anticyclonically rotated ridges, the sediment is eroded from the crests and the amplitude decreases. For this reason, only the modes with negative values of α tend to grow at a significant rate.

When the seabed is active only during a small part of the tidal cycle, as in Fig. 5.7 and 5.8, both cyclonically and anticyclonically rotated crests are allowed to grow. The physical explanation for this is in section 2.2.2. With increasing number of levels, and thus increasing the extent to which to flow has a vertical structure, the orientation of the modes changes. Two effects play an important role here.

The first is the Ekman veering: it turns out that this causes the crests of the modes to turn cyclonically, i.e. the value of α decreases for all modes. The second effect is the preferred cyclonic eccentricity of the near-bed tidal ellipse. This effect causes the absolute angle between the crests and the major axis of the tidal ellipse to increase. Modes with negative (positive) values of α become more thus negative (positive).

When the crests are cyclonically oriented, the two effects reinforce each other and the crests rotate further cyclonically when the number of levels is increased. In contrast, the two effects

counteract when the crests are anticyclonically oriented and their orientation changes only by a few degrees.

Figure 5.8b shows the presence of two modes that resemble the cyclonically and anticyclonically oriented long bed waves, despite the fact that the eccentricity of the depth-averaged tidal ellipse is zero. It turns out that the growth rates of the long bed waves grow with increasing number of levels because of the enhanced eccentricity of the tidal ellipse near the bed. The small value of the eccentricity, $\varepsilon = 0.019$ in the bottom level, is enough for long bed waves to forms. With $\varepsilon = 0$ in the bottom level, no long bed waves are found, explaining why the two modes are not found in the output of the one-level model (Fig. 5.8b). It must be noted that the tidal currents near the bed are almost never exactly rectilinear.

As for the decreasing growth rates when the spring-neap cycle is introduced, this can be explained as follows. In the case of the single harmonic, the maximum tidal flow velocity in the bottom level (0.513 m s^{-1}) is just above the threshold value for sediment movement ($\sim$0.494 m s^{-1}). The sediment transport, being proportional to the difference between the tidal flow velocity and the threshold value for sediment movement, then takes place during each M_2-tidal cycle. When the model is implemented with the spring-neap cycle, the maximum difference between the tidal velocity and the threshold value for erosion is fixed since $U_{da} = U_{S_2} + U_{M_2}$ is fixed. However, the maximum total tidal flow velocity in the bottom level only reaches values above the threshold value for sediment movement during the spring phase of the spring-neap cycle. Since the sediment transport is averaged over the full spring-neap cycle, the tidally averaged sediment transport and therefore the growth rates are reduced greatly.

For stronger elliptical tides, distinguishable modes merge into one mode when the spring-neap cycle is introduced. In case of the single harmonic the maximum flow during one cycle of the M_2-tide is constant (0.9 m s^{-1}), giving rise to residual circulation for very specific values of λ. In the case of the spring-neap cycle, this maximum flow varies between 0.46 m s^{-1} during the neap phase and 0.9 m s^{-1} during the spring phase. Not only does this result in lower growth rates, also the residual circulation is found for a wide range of values of λ.

6.2 Different Values of the Vertical Eddy Viscosity

The value of the vertical eddy viscosity A_v has been chosen following Bowden (1953). Model runs have been made considering values of A_v which are halve and ten times the default value. For high values, the multilevel model mimics the one-level model and the results are similar.

For small values of A_v, the vertical structure of the tide is enhanced. An example is in Fig. 6.1 which is a colour plot of the growth rates as a function of K and α for model run 3a with $N = 35$ and with A_v half of the default value. If one compares this with Fig. 5.7, it is evident that the wavelengths and orientation of the modes do not change significantly. As for the growth rates: they increase (decrease) for small (large) wavelengths. Also, more bed perturbations with positive growth rate are found for positive values of α, explained by the enhanced eccentricity of the tidal ellipse near the bottom ($\varepsilon_{da} = 0.456$).

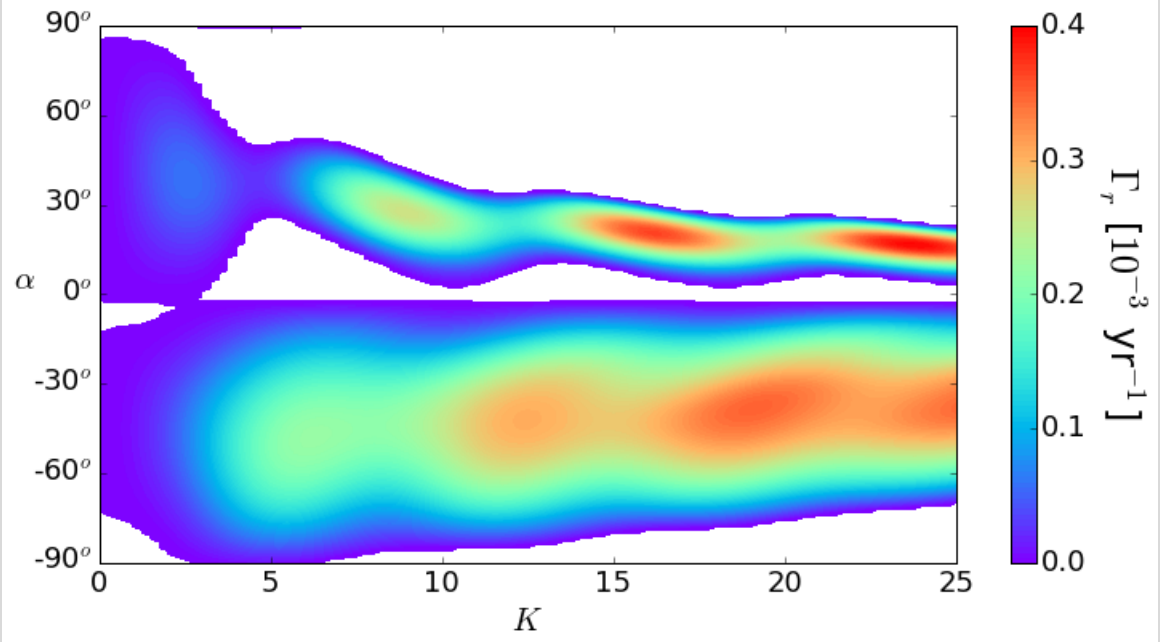

Figure 6.1: Same as Fig. 5.7, except with A_v half the default value.

6.3 Model Limitations

In this study, the tidal flow has been modelled for multiple levels. The interaction between the levels was through vertical shear. Fluid exchange between the levels was not allowed, setting the vertical flow velocity to zero. This is the first major difference between the model presented here and the one used by Hulscher (1996). Circulation in the vertical plane plays an important role in the initial formation of bed forms with small wavelengths. Therefore the current model is not able to reproduce bed forms such as sand waves.

A limitation in the use of linear stability analysis is that it only gives insights in the initial formation of tidal sand ridges. No information about the finite amplitude of bed forms of their equilibrium shape is obtained. For this, it would be necessary to include (weakly) nonlinear effects in the model. This was done for a depth-averaged model by Roos et al. (2004). It remains a challenge for multi-level models.

As in most studies using an idealized model (amongst others Huthnance, 1982, Hulscher et al., 1993, Hulscher, 1996, Blondeaux et al., 2009), stratification effects are not considered: the water density ρ is assumed to be constant. According to Maas and Van Haren (1987), stratification effects produce an additional vertical phase shift in the tidal flow. The Ekman layer depth of the cyclonically rotating velocity vector (see Appendix A) is so small that density differences within this layer are negligible. In contrast, the Ekman layer of the anticyclonically rotating velocity vector, having a greater depth, can be affected by a density jump, which is believed to suppress turbulent motions and affect the phase ϕ_-. Maas and Van Haren (1987) calculated a phase jump of approximately 30^o for ϕ_- for stratified circumstances, which is in

accordance with the observed phase jump. It would be difficult to include stratification effects into the model, since stratification is by no means constant in time, depending on for example wind stress and advection.

Also, the sea bed is assumed to be composed of cohesionless sediment of uniform size. However, natural sediments always consist of particles with different grain sizes. This size of a sediment particle greatly influences the critical Shields parameter for sediment movement and the transport move of the particle: bedload transport is the dominant mode for large grain sizes and small suspended load transport for smaller grain sizes. The effect of different grain sizes on the formation of tidal sand ridges has been studied using an depth-averaged model by Walgreen et al. (2004) and Roos et al. (2007). It remains a challenge for multi-level models. Based on this, and for reasons of feasibility, the present study assumes cohesionless sediment of uniform size.

The model assumes a flat horizontal bottom on which bed forms such as tidal sand ridges and long bed waves can grow. Any effects of sloping bottom configurations or coasts are ignored. Also, the effect of tidal constituents (such as the M_0- and M_4-tide) that can cause bed form migration are neglected.

7 Conclusions

This thesis has focused on tidal sand ridges and long bed waves in coastal seas. The following research questions were considered:

1. What is the effect of the linearization of the bed shear stress on the length scale and orientation of tidal sand ridges and long bed waves in the initial stages of development?
2. Are the properties of tidal sand ridges and long bed waves sensitive to changing water depth?
3. (a) Can the vertical structure of the tidal currents explain the difference between modelled and observed orientation of long bed waves?
   (b) Is weak elliptical tidal flow necessary for long bed waves to form?
4. How does the spring-neap cycle affect the properties of the bed forms?

The answers to these questions will be given in the subsequent sections. A morphodynamic model has been developed to study the relation between the characteristics of bed forms and the environmental conditions, such as local water depth and tidal conditions. The model used combines the vertical structure of the tide with a sophisticated sediment transport formulation.

7.1 Linearization of Bed Shear Stress

The working hypothesis was that the properties of the modelled tidal sand ridges and long bed waves are the same for linearized and quadratic bed shear stress. The results showed that if the bed shear stress is linearized, the modelled tidal sand ridges and long bed waves do not change significantly with respect to the those found with a model that uses quadratic bed shear stress. The largest change in wavelength and orientation of the fastest growing mode between linearized and quadratic bed shear stress is about 0.1 kilometer and 4 degrees, respectively. This difference is smaller for the other modes.

7.2 Changing Water Depth

The working hypothesis for this research question was that tidal sand ridges are most likely to form when the local water depth in between 30 and 40 meters.

Increasing water depth appears to have several effects on the geometrical characteristics of the tidal sand ridges. First of all, their crests rotate cyclonically: the difference in orientation is in the order of 14^o. Secondly, the maximum tidal flow velocity is proportional to the local water depth, which has an effect on the crest-to-crest distance: in relative deep seas, this distance is larger. Also, anticyclonically oriented ridges are more likely to form in shallow seas since the maximum tidal flow is then just above the threshold value for erosion.

The initial growth rates of the tidal sand ridges also depends on the local water depth. It turns out that there is an optimum depth at which the tidal sand ridges grow fastest. For the tidal conditions used in this study, the maximum growth rate of tidal sand ridges is found for a local water depth of ~ 60 meter.

7.3 Vertical Structure of the Tidal Currents

7.3.1 Orientation of Long Bed Waves

The working hypothesis of this study was that Ekman veering can explain the discrepancy in observed and modelled orientation of long bed waves. The result is that inclusion of the vertical structure of the tide improves the orientation of the modelled long bed waves.

The multilevel model developed in this study is able to reproduce the vertical structure of the tidal flow: the maximum tidal flow velocity near the surface is larger than that near the bottom and is also the time of maximum flood current increases from bottom to surface. Ekman veering, turning of the tidal flow direction with depth, is also included. Furthermore, the model correctly simulates the enhanced eccentricity of the tidal ellipse near the bottom.

As for the formation of tidal sand ridges and long bed waves, several conclusions can be made regarding the effect of the vertical structure of the flow. By including this, ridges with a wider range of geometrical characteristics (orientations and wavelength) are allowed to grow, mainly for small wavelengths. Also, the growth rates increase.

When the maximum tidal flow is just above the threshold value for erosion, long bed waves are most likely to form. Ekman veering and enhanced eccentricity of the near-bed tidal ellipse causes bed forms to rotate. The former has the effect of increasing (decreasing) the angle of the cyclonically (anticyclonically) oriented ridges with the tidal currents. The effect of the latter is increasing this angle for both cyclonically and anticyclonically oriented ridges.

For the cyclonically oriented ridges, the two effects reinforce each other and the angle between their crests and the tidal flow increases by about 25 degrees. However, the angle for the anticyclonically oriented ridges only by a few degrees since the two effects counteract in this case.

7.3.2 Formation of Long Bed Waves

The hypothesis was that long bed waves only form when the maximum tidal flow velocity is just above the threshold value for erosion and when the eccentricity of the tidal ellipse is above 0.2.

The results presented in this study suggest that both cyclonically and anticyclonically can also form when the depth-averaged eccentricity is set to zero. In this case, a small eccentricity near the bed is created when the vertical structure of the tidal currents is introduced. It turns out that small values (0.02) of the eccentricity near the bed are sufficient for long bed wave formation when the maximum tidal flow velocity is just above the threshold value for erosion.

As for the maximum tidal flow velocity. When this is increased, the results show that anticyclonically oriented long bed waves are no longer allowed to grow. Cyclonically oriented long bed waves can only grow for elliptical tidal currents.

7.4 Spring-Neap Cycle

The working hypothesis was that the spring-neap cycle has no effect on the properties of the tidal sand ridges and long bed waves. The results show that, when the spring-neap cycle is included in the model, the growth rates decrease. This effect is especially important for the case of weak tidal flow. However, the spring-neap cycle has little effect on the wavelengths and orientations of the modelled tidal sand ridges and long bed waves. Only for strong elliptical tidal flows, when several distinguishable modes merge, the spring-neap cycle has effect because of the varying maximum tidal currents during the spring-neap cycle.

A

Vertical Structure of the Tidal Ellipse

The Coriolis force has an important effect on the oscillatory tidal currents, which makes the behaviour of tidal flow rather complicated. It turns out that both the phase and direction of the current vary with height, giving rise to time-dependent veering. Here, the amplitude and phase of both the u-component and the v-component of the tidal flow are used to construct the representative tidal ellipse. The method to construct the ellipse is described in detail in Prandle (1982), Johns (1983) and Maas and Van Haren (1987) and is discussed to some extent here.

Each ellipse can be constructed by two opposite rotating circular vectors, an example is shown in Fig. A.1. The red and blue circles represent with frequency ω cyclonic and anticyclonic rotating velocity vectors with different but constant magnitudes on the northern hemisphere. The two motions combine to give a velocity vector which describes an ellipse. The properties of the ellipse can be derived from the clockwise and anticlockwise components. The direction of rotation of the circle with the largest radius determines the direction of rotation of the ellipse. The characteristics to be determined from the ellipse are:

- Length of semi-major axis (U_a: maximum current velocity)
- Length of semi-minor axis (U_b: minimum current velocity)
- Ellipticity (ε: eccentricity of tidal ellipse)
- Inclination (Φ: angle between $x-$axis and semi-major axis)
- Phase (Θ: angle between initial orientation of tidal current and semi-major axis)

For the periodic oscillation of angular frequency ω motion at any level z, the velocity components U, V in the x, y-direction can be written as

$$U = \Re\{\hat{u}e^{-\mathrm{i}\omega t}\} = u_c \cos\omega t + u_s \sin\omega t = A_u \cos(\omega t - \phi_u), \tag{A.1a}$$

$$V = \Re\{\hat{v}e^{-\mathrm{i}\omega t}\} = v_c \cos\omega t + v_s \sin\omega t = A_v \cos(\omega t - \phi_v), \tag{A.1b}$$

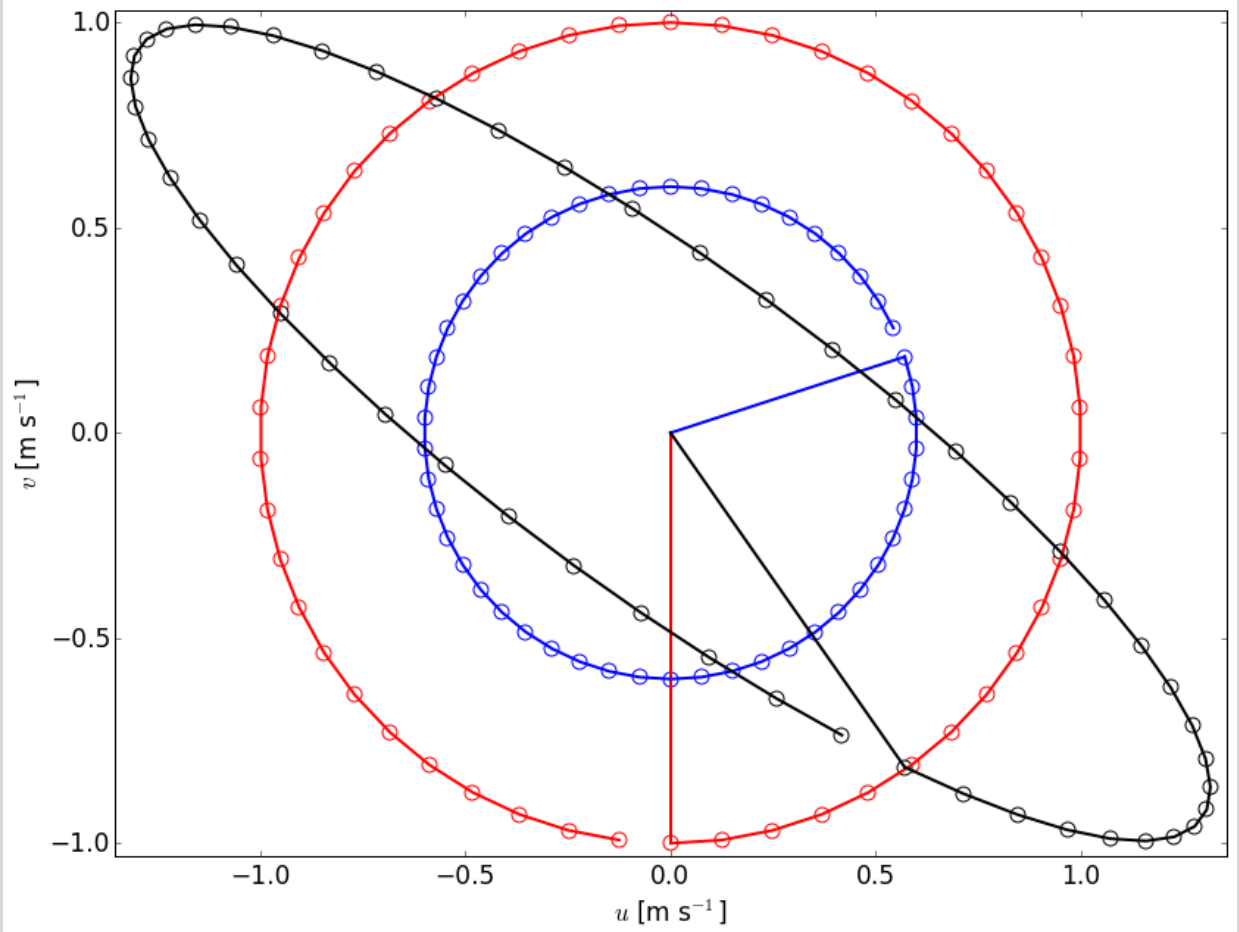

Figure A.1: An example of the construction of an ellipse from two circular counter-rotating vectors. Black: constructed ellipse. Red: Anti-clockwise rotating circular vector. Blue: Clockwise rotating circular vector.

with

$$\begin{aligned} \phi_u &\equiv \arctan\left(\frac{u_s}{u_c}\right), \quad A_u \equiv \frac{u_s}{\sin\phi_u} = \frac{u_c}{\cos\phi_u}, \\ \phi_v &\equiv \arctan\left(\frac{v_s}{v_c}\right), \quad A_v \equiv \frac{v_s}{\sin\phi_v} = \frac{v_c}{\cos\phi_v}, \end{aligned} \tag{A.2}$$

where u_c, u_s, v_c, v_s, A_u and A_v are (real) amplitudes. Variables ϕ_u and ϕ_v represent the phase lags for both velocity components. Note that the amplitude and the phase vary with z. The velocity vector (U, V) can be written as a complex velocity Q:

$$Q = U + \mathrm{i}V. \tag{A.3}$$

When Q is drawn in a complex plane, an ellipse is obtained. The rewriting of Q clarifies how

an ellipse is constructed out of two counter-rotating vectors.

$$\begin{aligned} Q &= A_u \cos\omega t - \phi_u + \mathrm{i} A_v \cos\omega t - \phi_v = \\ &= A_u \frac{e^{\mathrm{i}(\omega t - \phi_u)} + e^{-\mathrm{i}(\omega t - \phi_u)}}{2} + \mathrm{i} A_v \frac{e^{\mathrm{i}(\omega t - \phi_v)} + e^{-\mathrm{i}(\omega t - \phi_v)}}{2} = \\ &= \frac{A_u e^{-\mathrm{i}\phi_u} + \mathrm{i} A_v e^{-\mathrm{i}\phi_v}}{2} e^{\mathrm{i}\omega t} + \frac{A_u e^{\mathrm{i}\phi_u} + \mathrm{i} A_v e^{\mathrm{i}\phi_v}}{2} e^{-\mathrm{i}\omega t} = \\ &= w_+ e^{\mathrm{i}\omega t} + w_- e^{-\mathrm{i}\omega t}, \end{aligned} \tag{A.4}$$

with

$$w_+ \equiv \frac{A_u e^{-\mathrm{i}\phi_u} + \mathrm{i} A_v e^{-\mathrm{i}\phi_v}}{2} = \frac{(u_c + v_s) + \mathrm{i}(v_c - u_s)}{2}, \tag{A.5a}$$

$$w_- \equiv \frac{A_u e^{\mathrm{i}\phi_u} + \mathrm{i} A_v e^{\mathrm{i}\phi_v}}{2} \quad = \frac{(u_c - v_s) + \mathrm{i}(v_c + u_s)}{2}. \tag{A.5b}$$

The quantities $w_+ e^{\mathrm{i}\omega t}$ and $w_- e^{-\mathrm{i}\omega t}$ represent the cyclonic and anticyclonic rotating velocity vectors. Combined, the two motions describe the tidal ellipse. At this point, it is convenient to rewrite the complex characteristics w_+, w_- in their polar form.

$$w_+ = R_+ e^{\mathrm{i}\phi_+}, \tag{A.6a}$$

$$w_- = R_- e^{\mathrm{i}\phi_-}. \tag{A.6b}$$

Here, $R_{+,-}$ and $\phi_{+,-}$ represent the radii and phases of the cyclonic and anticyclonic rotating velocity vectors, respectively. They are

$$R_{+,-} \equiv \sqrt{\Re(w_{+,-})^2 + \Im(w_{+,-})^2}, \tag{A.7a}$$

$$\phi_{+,-} \equiv \arctan\left(\frac{\Im(w_{+,-})}{\Re(w_{+,-})}\right). \tag{A.7b}$$

Now

$$Q = R_+ e^{\mathrm{i}(\omega t + \phi_+)} + R_- e^{-\mathrm{i}(\omega t - \phi_-)}. \tag{A.8}$$

To determine the relations for the characteristics of interest in terms of characteristics $R_{+,-}$ and $\phi_{+,-}$, it is assumed that ϕ_+ and ϕ_- have values in the range $[-\pi, \pi)$. The relation for the phase of the ellipse can be found for the moment that the two circular vectors are aligned. The phase is proportional to the time needed for the current to reach its maximum value (t_{max}) and Eq. A.8 shows that t_{max} is reached when

$$\omega t + \phi_+ = -\omega t + \phi_- + 2k\pi, \quad \text{with } k = 0, \pm 1, \pm 2, \ldots \tag{A.9}$$

The phase Φ is thus defined as

$$\Phi = \omega t_{max} = \frac{\phi_- - \phi_+}{2} + k\pi. \tag{A.10}$$

At $t = t_{max}$, the current reaches its maximum value Q_{max}. A relation for the length of semi-major axis U_a is obtained by substituting Eq. A.10 into Eq. A.8.

$$\begin{aligned} Q_{max} &= R_+ e^{\mathrm{i}(\omega t_{max}+\phi_+)} + R_- e^{-\mathrm{i}(\omega t_{max}-\phi_-)} = \\ &= R_+ e^{\mathrm{i}(\frac{\phi_-+\phi_+}{2}+k\pi)} + R_- e^{\mathrm{i}(\frac{\phi_-+\phi_+}{2}-k\pi)} = \\ &= (R_+ + R_-) e^{\mathrm{i}(\frac{\phi_-+\phi_+}{2}+k\pi)}. \end{aligned} \tag{A.11}$$

The maximum current, corresponding to the semi-major axis of the ellipse, is therefore

$$U_a = R_+ + R_-. \tag{A.12}$$

Likewise, the minimum current, corresponding to the semi-minor axis, is

$$U_b = R_+ - R_-. \tag{A.13}$$

If $U_b > 0$ ($U_b < 0$), the velocity vector rotates cyclonic (anticyclonic). The ratio of the lengths of the semi-major and semi-minor axis define the ellipticity of the ellipse:

$$\varepsilon = \frac{U_b}{U_a} = \frac{R_+ - R_-}{R_+ + R_-}. \tag{A.14}$$

The orientation of the semi-major axis or inclination of the ellipse is

$$\Theta = \frac{-\phi_- - \phi_+}{2} + k\pi. \tag{A.15}$$

The characteristics that describe the tidal ellipse are derived from the velocity components U, V. Since U and V are functions of the vertical coordinate z, so are the characteristics. An example of this is shown in Fig. A.2. The depth-averaged values of the characteristics are indicated by the dotted line.

Fig. A.2 shows a typical logarithmic vertical profile for the semi-major axis of the ellipse. The bed-shear stress explains this increase of the maximum current velocity with height. The increasing phase is explained by the effect of friction near the bottom, which is greater than inertia; further away from the bottom, friction becomes weaker and inertia becomes more prevalent. The inclination of the flow can both increase and decrease with height.

The vertical structure of eccentricity is more complex and is determined by the Ekman-layer thickness of each one of the two circular vectors. The Ekman-layer thickness of the cyclonic and anticyclonic components are

$$\delta_+ = \sqrt{\frac{2A_v}{\omega + f}}, \tag{A.16a}$$

$$\delta_- = \sqrt{\frac{2A_v}{\omega - f}}, \tag{A.16b}$$

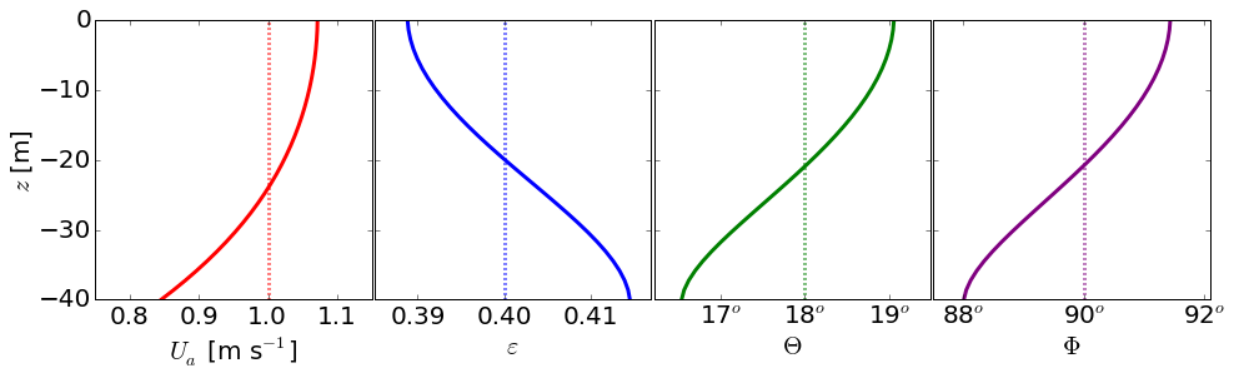

Figure A.2: An example of how the characteristics of an tidal ellipse vary with depth (Solid lines). From left to right: semi-major axis, eccentricity, inclination and phase. Dotted lines: depth-averaged values.

in which A_v is the vertical eddy viscosity coefficient (Prandle, 1982). From this, it follows that the vertical scale of the cyclonic component is compressed relative to the clockwise component. In the lower part of the flow, the cyclonic component therefore dominates and the tidal ellipse is polarised cyclonic. In the top part of the flow, the anticyclonic flow is more dominant than in the lower part. The eccentricity of the flow therefore increases with height.

Note that in the northern hemisphere $(\omega + f)$ is always positive and that $(\omega - f)$ can be both positive and negative. For convenience, without lose of generality, the latitude is limited to values which keep $(\omega - f)$ positive. For the M_2-tide on the northern hemisphere, this means latitudes south of 74^{o}N.

Bibliography

Blondeaux, P., De Swart, H. E. and Vittori, G. (2009), 'Long bed waves in tidal seas: an idealized model', *Journal of Fluid Mechanics* **636**, 485–495.

Bowden, K. (1953), 'Note on wind drift in a channel in the presence of tidal currents', *Royal Society of London Proceedings Series A* **219**(1139), 426–446.

Bowden, K. F. (1983), *Physical oceanography of coastal waters*, Ellis Horwood Ltd., Chichester England.

Dyer, K. (1986), 'Coastal and estuarine sediment dynamics.', *Chichester: Wiley* .

Dyer, K. R. and Huntley, D. A. (1999), 'The origin, classification and modelling of sand banks and ridges', *Continental Shelf Research* **19**(10), 1285–1330.

Einstein, H. A. (1950), *The bed-load function for sediment transportation in open channel flows*, number 1026, US Department of Agriculture.

Fredsøe, J. and Deigaard, R. (1992), *Mechanics of coastal sediment transport*, Vol. 3, World scientific.

Hulscher, S. J. (1996), 'Tidal-induced large-scale regular bed form patterns in a three-dimensional shallow water model', *Journal of Geophysical Research. Pt. C: Oceans* **101**(C9), 20727–20744.

Hulscher, S. J., de Swart, H. E. and de Vriend, H. J. (1993), 'The generation of offshore tidal sand banks and sand waves', *Continental Shelf Research* **13**(11), 1183–1204.

Huthnance, J. M. (1982), 'On one mechanism forming linear sand banks', *Estuarine, Coastal and Shelf Science* **14**(1), 79–99.

Johns, B. (1983), *Physical oceanography of coastal and shelf seas*, Elsevier.

Knaapen, M. A., Hulscher, S., Vriend, H. J. and Stolk, A. (2001), 'A new type of sea bed waves', *Geophysical Research Letters* **28**(7), 1323–1326.

Kovacs, A. and Parker, G. (1994), 'A new vectorial bedload formulation and its application to the time evolution of straight river channels', *Journal of Fluid Mechanics* **267**, 153–183.

Lorentz, H. A. et al. (1926), 'Verslag staatscommissie zuiderzee 1918–1926', *Algemene Landsdrukkerij,'s-Gravenhage* pp. 1–345.

Maas, L. and Van Haren, J. (1987), 'Observations on the vertical structure of tidal and inertial currents in the central north sea', *Journal of Marine Research* **45**(2), 293–318.

Meyer-Peter, E. and Müller, R. (1948), Formulas for bed-load transport, IAHR.

Off, T. (1963), 'Rhythmic linear sand bodies caused by tidal currents', *AAPG bulletin* **47**(2), 324–341.

Prandle, D. (1982), 'The vertical structure of tidal currents', *Geophysical & Astrophysical Fluid Dynamics* **22**(1-2), 29–49.

Pugh, D. T. (1996), *Tides, surges and mean sea-level*, John Wiley & Sons Ltd.

Reeve, D., Chadwick, A. and Fleming, C. (2004), *Coastal engineering: processes, theory and design practice*, CRC Press.

Roos, P. C., Hulscher, S. J., Knaapen, M. A. and Van Damme, R. M. (2004), 'The cross-sectional shape of tidal sandbanks: Modeling and observations', *Journal of Geophysical Research: Earth Surface (2003–2012)* **109**(F2).

Roos, P. C., Wemmenhove, R., Hulscher, S. J., Hoeijmakers, H. W. and Kruyt, N. (2007), 'Modeling the effect of nonuniform sediment on the dynamics of offshore tidal sandbanks', *Journal of Geophysical Research: Earth Surface (2003–2012)* **112**(F2).

Seminara, G. (1998), 'Stability and morphodynamics', *Meccanica* **33**(1), 59–99.

Shennan, I., Lambeck, K., Flather, R., Horton, B., McArthur, J., Innes, J., Lloyd, J., Rutherford, M. and Wingfield, R. (2000), 'Modelling western North Sea palaeogeographies and tidal changes during the Holocene', *Geological Society, London, Special Publications* **166**(1), 299–319.

Shields, A. (1936), Application of similarity principles and turbulence research to bed-load movement, Technical report, Soil Conservation Service.

Soulsby, R. (1997), *Dynamics of marine sands: a manual for practical applications*, Thomas Telford.

Talmon, A., Struiksma, N. and Van Mierlo, M. (1995), 'Laboratory measurements of the direction of sediment transport on transverse alluvial-bed slopes', *Journal of Hydraulic Research* **33**(4), 495–517.

van de Meene, J. W. H. (1994), The shoreface-connected ridges along the central Dutch coast, PhD thesis, Universiteit Utrecht.

van Dijk, T. A., Lindenbergh, R. C. and Egberts, P. J. (2008), 'Separating bathymetric data representing multiscale rhythmic bed forms: A geostatistical and spectral method compared', *Journal of Geophysical Research: Earth Surface (2003–2012)* **113**(F4).

Van Lancker, V. R., Bonne, W. M., Garel, E., Degrendele, K., Roche, M., Van den Eynde, D., Bellec, V. K., Brière, C., Collins, M. B. and Velegrakis, A. F. (2010), 'Recommendations for the sustainable exploitation of tidal sandbanks', *Journal of Coastal Research* pp. 151–164.

Walgreen, M., De Swart, H. E. and Calvete, D. (2004), 'A model for grain-size sorting over tidal sand ridges', *Ocean Dynamics* **54**(3-4), 374–384.

Wu, Z., Jin, X., Cao, Z., Li, J., Zheng, Y. and Shang, J. (2010), 'Distribution, formation and evolution of sand ridges on the East China Sea shelf', *Science in China Series D: Earth Sciences* **53**(1), 101–112.

Zimmerman, J. (1981), 'Dynamics, diffusion and geomorphological significance of tidal residual eddies', *Nature* **290**, 549–555.